Review

Tianji Liu, Rongyang Xu, Peng Yu, Zhiming Wang and Junichi Takahara*

Multipole and multimode engineering in Mie resonance-based metastructures

https://doi.org/10.1515/nanoph-2019-0505
Received December 7, 2019; revised January 30, 2020; accepted January 30, 2020

Abstract: Benefited from the well-known Mie resonance, a plethora of physical phenomena and applications are attracting attention in current research on dielectric-based nanophotonics. High-index dielectric metastructures are favorable to enhance light-matter interaction in nanoscale with advantages such as low loss, optical magnetism, and multipolar responses, which are superior to their plasmonic counterpart. In this review, we highlight the important role played by Mie resonance-based multipolar and multimodal interaction in nanophotonics, introducing the concept of "multipole and multimode engineering" in artificially engineered dielectric-based metastructures and providing an overview of the recent progress of this fast-developing area. The scope of multipole and multimode engineering is restricted not only in multipolar interferences of meta-atom and meta-molecule but also in the nontrivial intermodal coupling (Fano resonance and bound states in the continuum), in the collective mode and the surface lattice mode appearing via periodic meta-lattices and aperiodic meta-assembly, in chiral enhancement via chiral and achiral dielectric metastructures, and in Mie resonance-mediated hybrid structures (Mie-plasmon and Mie-exciton). Detailed examples and the underlying physics of this area are discussed in-depth, in order to lead the multifunctional metastructures for novel applications in the future.

Keywords: Mie resonance; dielectric metamaterials; dipole family; chirality; strong coupling.

1 Introduction

In 1908, German physicist Gustav Mie gave the solution of Maxwell's equations while he was analyzing the scattering problem of wavelength-comparable particles (e.g. gold nanoparticle) in a homogeneous surrounding (e.g. water) under the excitation of electromagnetic plane wave, which afterward was well known as the Mie solution [1, 2] A century later, the current research of ubiquitous scattering phenomena in artificially engineered micro/nanostructures has been actively developing from the start point of Mie scattering. Photonic crystals [3], plasmonics [4], plasmonic metamaterials [5], and dielectric metamaterials [6] continuously challenge our common wisdom, expand the boundary of science and technology, and facilitate the advancement of interdisciplinary research. Among a wide range of artificial structures in photonics, we focus on high-index dielectric metastructures in this review. In contrast to photonic crystals, dielectric metastructures are not restricted in periodic arranged structures; the characteristic Mie resonant peaks can even be observed from one single structure. Moreover, out-of-plane excitation (normal incidence or oblique incidence) is conventionally used in dielectric metastructures, instead of in-plane excitation or propagation in photonic crystals. In contrast to plasmonic metastructures, low loss and optical magnetism (wavelength-sized structures in the visible range) in single dielectric structures are unique advantages of dielectric metastructures. For the choice of materials of building blocks in dielectric metastructures, several common high-index and low-loss materials are frequently used in the visible range, like Si, Ge, TiO_2. Similar to photonic crystals, a unit cell of dielectric metastructures (e.g. a particle) is typically wavelength sized ($d \sim \lambda/n$, where d is

***Corresponding author: Junichi Takahara,** Photonics Center, Graduate School of Engineering, Osaka University, 2-1 Yamadaoka, Suita, Osaka 565-0871, Japan, e-mail: takahara@ap.eng.osaka-u.ac.jp. https://orcid.org/0000-0002-3683-626X
Tianji Liu: Institute of Fundamental and Frontier Sciences, University of Electronic Science and Technology of China, Chengdu 610054, China; and Graduate School of Engineering, Osaka University, 2-1 Yamadaoka, Suita, Osaka 565-0871, Japan. https://orcid.org/0000-0002-5862-2449
Rongyang Xu: Graduate School of Engineering, Osaka University, 2-1 Yamadaoka, Suita, Osaka 565-0871, Japan
Peng Yu and Zhiming Wang: Institute of Fundamental and Frontier Sciences, University of Electronic Science and Technology of China, Chengdu 610054, China

the typical size of a dielectric particle, λ is the wavelength in free space, and n is the refractive index of dielectric), resulting in the breakdown of the quasi-static approximation. To accurately describe and thoroughly explain the scattering phenomenon of wavelength-sized homogeneous sphere, Mie solution is well-suited to analyze the scattered fields in near-field and far-field regions [7, 8], and the total scattering cross-section (C_{sca}) can be expanded into an infinite series of spherical multipolar terms (Mie expansion)

$$C_{sca} = \frac{2\pi}{k^2}\sum_m^{\infty}(2m+1)(|a_m|^2 + |b_m|^2), \quad (1)$$

where a_m and b_m are Mie coefficients of the mth-order electric and magnetic multipolar modes, respectively. k is the wavenumber. Electric dipole (ED, $\sim a_1^2$), magnetic dipole (MD, $\sim b_1^2$), electric quadrupole (EQ, $\sim a_2^2$), and magnetic quadrupole (MQ, $\sim b_2^2$) are the first four multipole terms in the Mie expansion [9]. In mathematics, multipole terms in the Mie expansion form a complete and orthogonal basis for the decomposition of the scattered fields. For a 100-nm-radius Si nanosphere in free space, the scattering spectra and the electric fields (E-fields) distributions of dipole and quadrupole modes at multipolar scattering peaks (P1–P4) are shown in Figure 1A. One can simply distinguish the contribution of ED, MD, EQ, and MQ from the Mie expansion of scattering spectra (color lines in Figure 1A) and from the orientation of E-fields (black arrow in the insets of Figure 1A). Note that a_m and b_m are the functions of the particle size and the refractive index difference between the particle and the surroundings. High-index particles embedded in low-index medium are favorable to improve the Mie scattering efficiency. At the resonance of each multipolar mode, the electromagnetic fields are strongly confined inside the particle and the remarkable enhancement is comparable to the plasmonic counterpart. In contrast, a broadened ED scattering peak ($P_{plasmon}$) is obtained from a 100-nm-radius Au nanosphere (Figure 1B), due to the strongly damped plasmon mode. The expansion results indicate the lack of MD (blue line in Figure 1B) and high-order magnetic multipole modes in subwavelength-sized metal nanoparticles at the visible and near-infrared regions. Enlightened by the simplest case of nanosphere, we should clarify that the Mie solution, which gives an exact solution for the case of spherical particles and a first-order approximation for the case of nonspherical particles [7], is merely a special case of standard multipole expansion in electromagnetics [10]. For readers who are interested in numerically addressing the scattering problem of arbitrary particles or particles array, the analytical framework is available elsewhere [11]. Additionally, originating from toroidal current configuration (currents flowing along the merdians of a fictitious torus), toroidal multipoles cannot be directly extracted from the standard electric and magnetic multipole expansion; the specific formulism and detailed interpretation are available elsewhere [12, 13].

Recently, the artificial manipulation of multipolar and multimodal properties in dielectric metastructures have been extensively reported in zero- (0D; e.g. single nanoparticle [14–18]), one- (1D; e.g. single nanowire and nanorods [19–23], two- (2D; e.g. meta-array [24–26], and even three- (3D; e.g. nanohelices [27, 28], metamaterials [29]) dimensional metastructures. Here, we mainly focus on 0D (single or few particles) and 2D (array) metastructures, due to their compact and simplified geometrical configuration. We unambiguously give the concept of multipole engineering, which indicates the manipulation of multipolar interaction under linearly polarized planar wave, such as near-field coupling and multipolar interference effect appearing in single or few metastructures (Figure 1C). Beyond multipole engineering, the concept of multimode engineering indicates the manipulation of interaction (e.g. weak and strong coupling) between multipolar terms and exotic optical modes or states, like cavity mode (bound mode), lattice (diffraction) mode, circular polarization, plasmon mode, exciton mode, and others (Figure 1C). In this review, we aim at the recent progress and provide an insightful overview on the aforementioned areas, highlighting the crucial role of multipole and multimode engineering in Mie resonance-based metastructures.

Based on the above concept of multipole and multimode engineering, this review is organized as follows: single and cluster metastructure (meta-atom and meta-molecule)-mediated multipolar interference phenomena, which are responsible for the generation of several novel dipole modes and their multipole family, are investigated in Section 2. Fano resonance and bound states in the continuum are also discussed as the nontrivial multimode coupling phenomena. In Section 3, we extend our discussions to planar meta-film, including periodic meta-lattice and aperiodic meta-assembly, revealing the importance of the collective coupling effect and surface lattice modes. In Section 4, we overview the multimode engineering in chiral photonics, including achiral and chiral metastructures. In Section 5, we discuss the recent advancement of hybrid metastructures, highlighting the resonant coupling phenomena in dielectric-plasmonic and Mie-excitonic systems. In Section 6, we summarize this review and present the outlook of this fast-developing research area.

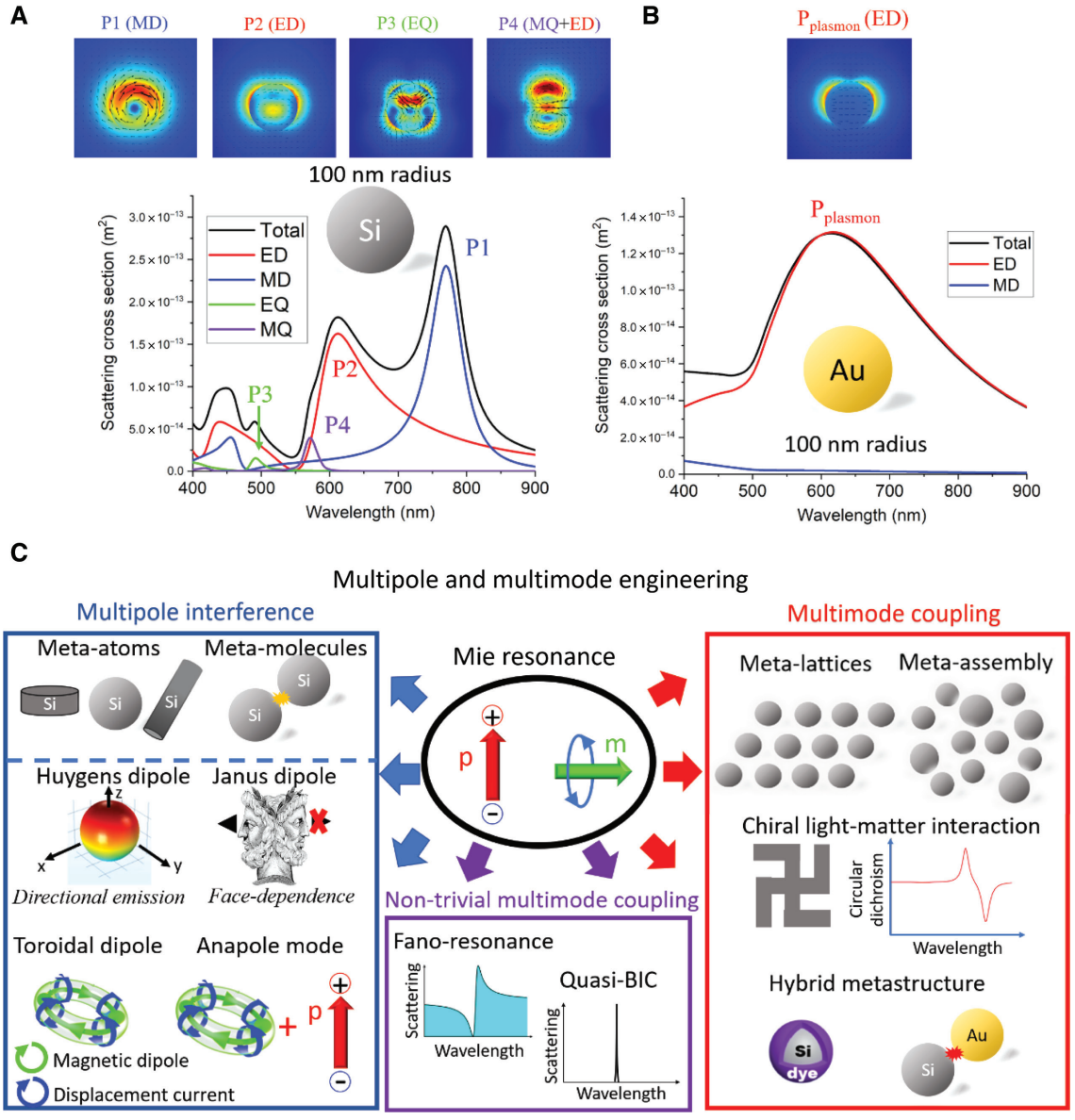

Figure 1: The introduction of multipole expansion and the concept of multipole and multimode engineering in metastructures. (A, B) The multipole expansion of scattering spectra in a 100-nm-radius Si nanosphere (A) and in a 100-nm-radius Au nanosphere (B). The contribution of dipole and quadrupole modes are given in (A), E-fields distribution at each peak of multipole modes are shown at the top of (A), black arrows denote the orientation of E-fields. The dominant ED mode and E-field distribution are shown in plasmonic nanoparticle (B). (C) The framework of this review, here we clearly distinguish Mie resonance-based multipole interference and multimode coupling phenomena. Meta-atoms and meta-molecules-mediated multipole interference phenomena include Huygens dipole, Janus dipole, toroidal dipole, anapole mode, and their high-order multipole modes. Multimode coupling includes the collective mode and the surface lattice mode in meta-lattices and meta-assembly, chiral light-matter interaction in achiral and chiral metastructures, and Mie-excitonic and Mie-plasmonic hybrid metastructures. Additionally, nontrivial multimode coupling includes Fano resonance and bound states in the continuum.

2 Multimode engineering in meta-atoms and meta-molecules

Recently, high-index dielectric single nanoparticle and cluster have attracted much attention in the photonic area [16] due to their clear physics and potential for multimodal engineering in the design of novel functional nanophotonic structure. Like atom and molecule operated as a basic constituent unit of matter, such an individual nanoparticle and single cluster are termed as “meta-atom” and “meta-molecule” in metastructures, respectively, highlighting their role as a structural unit in the interpretation of light-matter interaction (see Figure 1C). Although

the concept was initially proposed in plasmonics and metamaterials [30], we limit the discussion to high-index dielectric.

We firstly introduce the concept of multipole family frequently used in dielectric-based metastructures. The normal multipole family includes ED, MD, toroidal dipole (TD), and their high-order multipoles derived by multipole expansion or decomposition of the scattering fields; such an idea of decomposition deepens the understanding of complicated scattering fields generated by metastructures and has already been demonstrated via many applications according to the different engineering demands [31]. With the fast development of dielectric metastructures, multipole interference plays an important role in the engineering of the multipole family; recently, several types of extended multipoles have been proposed and demonstrated in dielectric-based metastructures by the superposition of normal multipole modes with different phase symmetry and vector structure, like Huygens dipole (HD), Janus dipole (JD), circular dipole (CD), anapole mode (AM), and their high-order multipoles. Such an engineered multipole family is dubbed as the "extended multipole family" and will be highlighted in this section, in order to distinguish their performance with that of the normal multipole family. The concept of extended multipole family is helpful for a better explanation of these gradually complicated physical phenomena in such a fast-developing area. We emphasize again that toroidal multipole mode and AM are associated with toroidal current configuration, which are not compatible to the framework of standard multipolar expansion (i.e. electric and magnetic multipoles). Besides, multipole family-based interparticle and intermodal coupling enables nontrivial but intriguing phenomena, such as Fano resonance and bound states in the continuum. Despite the complicated physical origin of the above normal and extended multipole family, a carefully designed Mie resonator (dielectric meta-atom or meta-molecule) provides a platform to improve their performance and enables them to be experimentally accessible in nanophotonics.

HD is composed of in-phase orthogonal ED moment ($\mathbf{p}$) and MD moment ($\mathbf{m}$) with equal intensities of induced dipole fields (i.e. $|\mathbf{p}| = |\mathbf{m}|/c$, c is speed of light in vacuum), releasing a unidirectional dipolar emission via satisfying the well-known Kerker condition (Figure 2A) [16, 32]. Usually, a simple subwavelength-sized plasmonic nanoparticle cannot be regarded as a HD source, due to the insufficient MD response in the visible range. Instead, a high-index Mie resonator is frequently used for unidirectional emission. HD is a powerful example to show the crucial phase symmetry in dipole interference (Figure 2A, B). Note that we mainly concern dipole and quadrupole interactions and skip a detailed discussion of other high-order multipoles in this section. Fundamentally, the electric fields induced by ED and MD (orthogonal arrangement) present even parity and odd parity, respectively, leading to constructive interference at one side but destructive interference at the other (red arrows in Figure 2B). Note that the realization of unidirectional emission is not restricted in HD, but other combinations like dipole-quadrupole (ED + EQ, MD + MQ) and quadrupole-quadrupole (EQ + MQ), which are attributed to the generalized Kerker effects in nanophotonics (Figure 2B) [16]. One special case is the superposition of dipole combinations (in-phase ED + MD) and antiphase quadrupole combinations (in-phase EQ + MQ), retaining only transverse scattering and suppressing both forward and backward scattering (Figure 2C) [33].

JD is composed of $\pi/2$ out-of-phase orthogonal ED mode and MD mode ($|\mathbf{p}|/c = |i\mathbf{m}|$) (Figure 2A), resulting in interesting face-dependent coupling or emission in adjacent nanophotonic structures (Figure 2A) [32]. Distinct with the well-known spin-momentum locking effect of CD (Figure 2D), JD does not show left-right directionality in adjacent dielectric slab. In contrast to HD or other generalized Kerker effect-based dipole combinations (Figure 2E), JD does not present the directionality in free space or far-field and the face dependence can be found only in adjacent evanescent-wave supporting waveguides, originating from the topology of complex vectorial electromagnetic fields in intermodal coupling (Figure 2F, G). Such face dependence is switchable by reversing the relative phase between ED and MD (i.e. from $\pi/2$ to $-\pi/2$; Figure 2F, G). Additionally, the introduction of helicity in JD (like CD) may form a novel type of dipole source termed "spinning JD," which effectively expands the scope of near-field directionality and combines with the spin-momentum locking phenomenon [34]. Practically, JD can be implemented by high-index Mie resonator (meta-atom) [34] or metal-dielectric-metal (plasmonic) resonator [35], which is promising for directional control in nanophotonic circuitry and quantum optics [36].

CD is composed of two $\pi/2$ out-of-phase orthogonal EDs, which is equivalent to point dipole with circular polarization in most functionalities (Figure 2A, D). Distinguished by rotational direction of dipole orientation, left-handed and right-handed CDs are crucial for the circular dichroism (CDC) [27], the spin-orbit interaction [37], and the spin-Hall effect of light [38]. Detailed discussions can be found in Section 4. HD, JD, and CD are inherently associated with near-field and far-field directionality, leading to the manipulation of the light flow via single

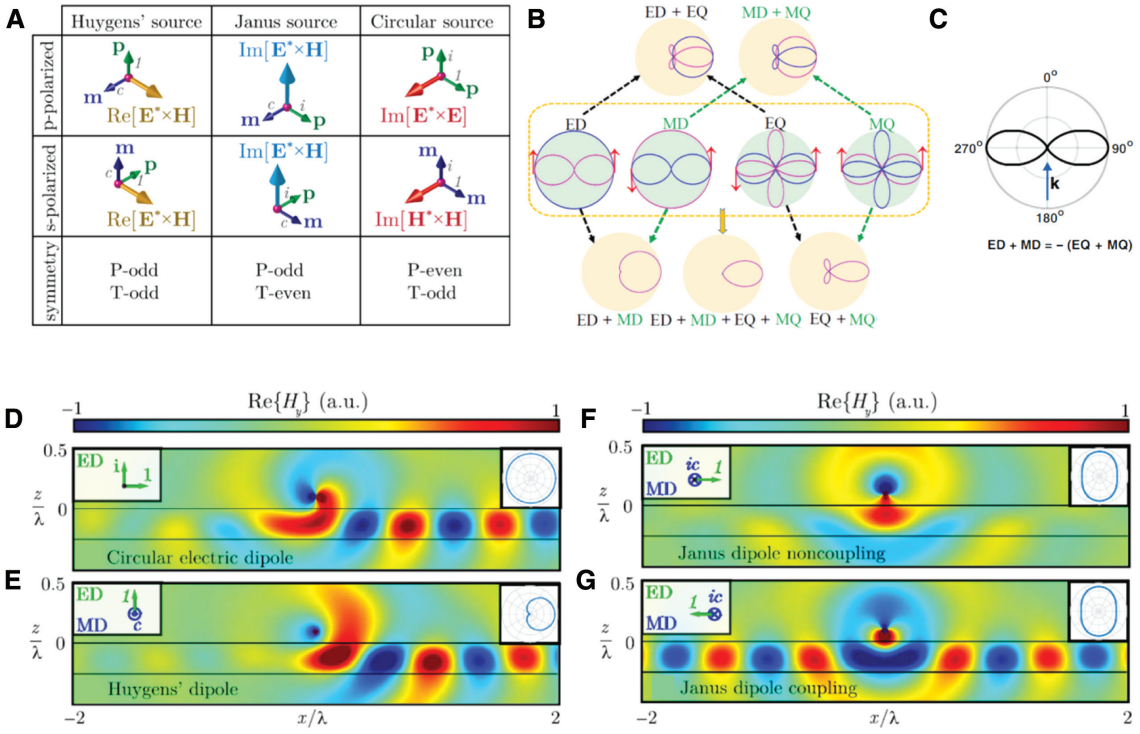

Figure 2: The application of extended multipole family.
(A) Comparison of HD, JD, and CD. Polarized and symmetrical configurations are shown (p-polarization, s-polarization, and parity-time [PT] symmetry). (B) The generalized Kerker condition is revealed by dipole and quadrupole interferences. The red arrows in the middle row show phase-parity of dipoles (ED, MD) and quadrupoles (EQ, MQ). The top and bottom rows give the examples of unidirectional radiation patterns by the superposition of dipoles and quadrupole. (C) Transverse scattering pattern by the superposition of dipole combinations (in-phase ED + MD) and antiphase quadrupole combinations (in-phase EQ + MQ). (D–G) The near-field directionality of CD, HD, and JD displayed in an adjacent thin dielectric slab. Physically, the spin-momentum locking of CD in (D). Unidirectional emission of HD in (E). Face-dependent noncoupling (F) and coupling (G) of JD. Adapted with permission from Refs. [16, 32, 33].

meta-atom mediated light-matter interaction in adjacent nanostructures.

Dynamic TD can be approximately interpreted as an azimuthally distributed MD (green circle in Figure 3A), produced by a displacement current (blue circle in Figure 3A) flowing along the meridians at the surface of imaginary torus (coil-like). Although the radiation patterns of TD mode in far-field are identical to ED mode (red grid in Figure 3A), the intrinsic difference between them is found in the near-field properties (i.e. the distinct distribution of E-fields). Therefore, several reports have argued that the TD (**T**) and its multipole family compose the third elementary dipole family (besides ED and MD), in order to emphasize its distinct parity-time symmetry (P-odd and T-odd) of dipole moment and charge-current configurations [39, 41]. However, the nonexistence and inexplicit meaning of TD and toroidal multipoles terms are clarified from complete spherical Mie expansion; therefore, TD can only be extracted from toroidal current expansion inside nanoparticle [42]. Different types of meta-molecules (meta-oligomer) are feasible to enhance TD in an all-dielectric configuration, such as trimer, tetramer, pentamer, and hexamer. In these meta-molecules, the rotational arrangement of nanoparticles is crucial to obtain high-quality factor (Q-factor) and enhanced TD mode (low transmission) [43, 44] (Figure 3B, C); interestingly, the fine tuning in the partial radius of Si nanodisk tetramers enables the further enhancement of the TD mode in meta-molecules, while the slightly breaking rotational symmetry results in the formation of trapped mode (dark mode-like) (Figure 3C, D) [40].

AM can be regarded as a nonradiating source (trapped mode) via destructive interference between the ED mode and the TD mode due to their identical far-field radiation patterns and out-of-phase configurations (Figure 4A) [42, 47–49]. Although such engineered anapole reveals vanishing far-field radiations (does not hold for all excitation directions [50]), one must note that AM is not an eigenmode of an open cavity (like multipole in Mie expansion) [51, 52]. In other words, the continuity of the boundary condition requires the existence of external excitation fields, implying the interaction of damping channels from different complex eigenmodes and holding the nonradiating

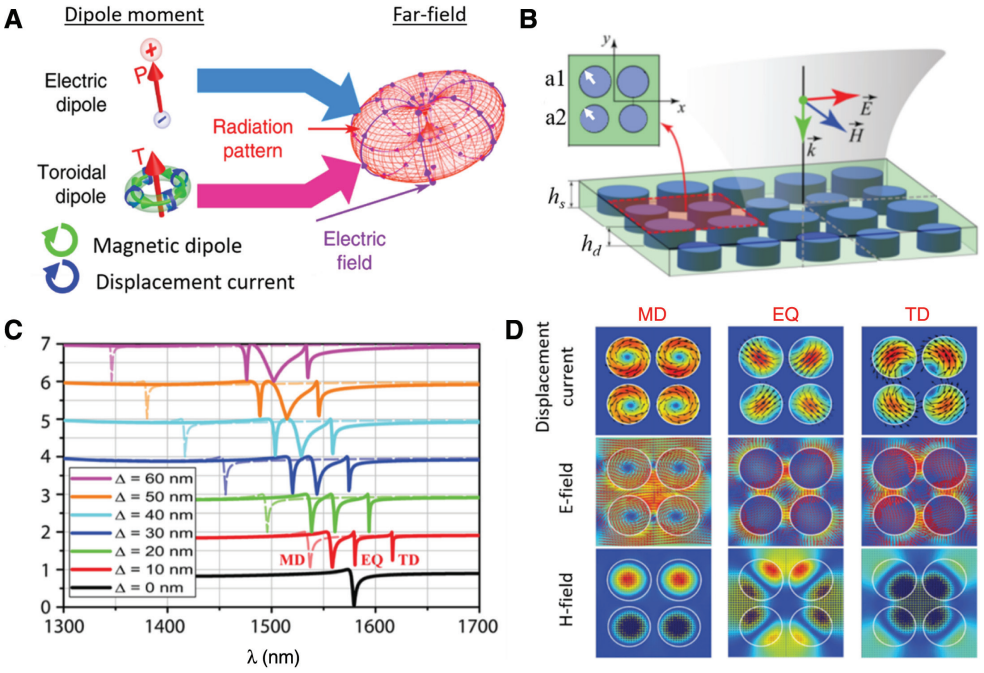

Figure 3: The application of TD mode.
(A) Comparison of electric dipole (ED) and TD, including the charge-current configuration and the radiation pattern in far-field. (B–D) Enhanced TD mode in Si-tetramer meta-molecule. The array of asymmetric meta-molecule composed of the fine tuning in the partial radius of Si nanodisk tetramers, Δ = a1–a2; a1 and a2 are the radius of unequal nanodisks in (B). (C) Transmission spectra of Si-tetramers with respect to Δ. (D) Distribution of displacement currents, E-field, and H-field in Si-tetramer, corresponding to Δ = 10 nm [red line in (C)]. Adapted with permission from Refs. [39, 40].

property only in steady state. But the intriguing zero-scattering property and well-confined stored electromagnetic energy in AM are still favorable for a plethora of applications in near-field and far-field, such as Purcell enhancement [45], anapole nanolaser [53], optical cloaking [54], and active nanophotonic devices [46]. As shown in Figure 4B–D [45], the first and the second orders of AM (AM1 and AM2) are supported in a single slotted Si nanodisk (see two dips of blue dotted line in Figure 4B), leading to multiresonance-based electromagnetic energy intensity (~$|E^2|$) enhancement exceeding 10^3 times. Although AM1 shows more suppressed scattering behavior than AM2 (Figure 4C), AM2 enables larger electromagnetic energy intensity generated by the combination of poloidal current mode and Fabry-Pérot (FP) mode (standing wave; Figure 4D); in contrast, AM1 is primarily a poloidal current mode (insets of Figure 4C). Moreover, the slotted geometry is accessible for the integration with quantum emitter or fluorescent substance. Realization of active control of AM is also important in nanophotonics; to this end, structured phase-change alloy $Ge_2Sb_2Te_5$ (GST) microdisks are demonstrated for multipolar Mie resonances and large mode shifting ($\Delta\lambda/\lambda \sim 15\%$) between ED and AM (Figure 4E) [46]. The dramatic change of optical constant during the phase transition in GST leads to an ED-AM switching, functionalizing a thermal-optical scattering mode convertor (bright mode-dark mode) in the infrared range.

Fano resonance is generally described as a physical phenomenon that a discrete localized state (weakly damping oscillator) destructively interferes with a continuum of states (strongly damping oscillator), accompanying a π-phase shift at the resonance of discrete state (Lorentz oscillator model) and producing an asymmetrical spectral line shape [55, 56]. Note that such line shape is controlled by Fano parameter (q) and external coupling from excitation (e.g. $q = 0$ and $q \to \infty$ correspond to uncoupled discrete state and continuum state, respectively); q is directly associated with the phase shift (δ) between the discrete state and a continuum by $q = \cot\delta$ (Figure 5A). In Mie resonant nanostructures, dipole-active mode and dipole-forbidden mode are frequently employed as bright mode (strongly damping) and dark mode (weakly damping) under the plane wave excitation, respectively. As demonstrated by Si heptamer (Figure 5B), magnetic resonance induced a phase difference between the center nanoparticle (blue line) and the outer ring (hexamer, black line), forming an individual dark mode and collective bright mode, respectively [57, 59]. The appearance of Fano-dip in scattering

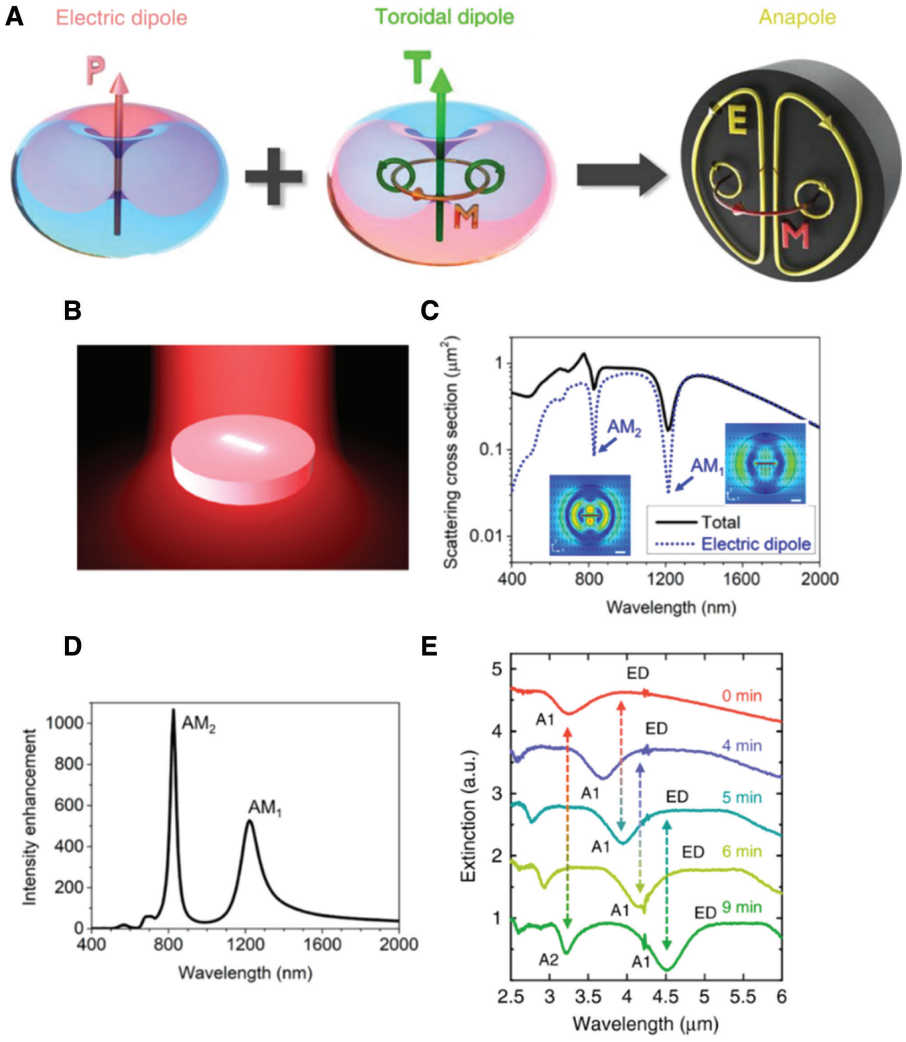

Figure 4: The application of AM.
(A) Formation of AM. Destructive interference between ED and TD leads to total scattering cancelation in far-field. (B–D) The first-order (AM1) and the second-order (AM2) AM excited in the slotted Si nanodisk. Scattering spectra (C), E-field distribution at the resonance of AM1 and AM2 [insets of (C)] and intensity enhancement (D) are shown. (E) Mode shifting in GST microdisk with respect to annealing time. Adapted with permission from Refs. [42, 45, 46].

spectra manifests the small q value and out-of-phase bright mode ($\delta \sim \pi/2$). Interestingly, less sensitive dependence on interparticle separations is shown in Si heptamer than their plasmonic counterpart. The occurrence of Fano resonance is not limited in meta-molecules, but even in a single Si nanorod (Figure 5C) [58, 60]. Two types of resonant modes, including Mie modes and FP modes, coexist in such nanorod with a large aspect ratio. Asymmetrically sharp Fano peak appears at $\lambda = 670$ nm due to the well-confined HE^{3}_{11} FP mode overlapping a broad background of Mie modes. For applications, refractive index sensing [61, 62] and electromagnetically induced transparency (a special type of Fano resonance characterized by $q = 0$ and almost the same resonant frequency in bright mode and dark mode) [63] are attractive in near-field coupling control due to their unique properties.

As another type of nonradiating state in photonics, bound states in the continuum (BIC) is revisiting and attractive to obtain the infinite Q-value (divergent lifetime) and energy trapping state in dielectric metastructures [47]. Implied by the name, BIC can be interpreted as a bound state coexisting with a radiation continuum (extended wave) at a certain frequency in an open system, but the bound state is still spatially confined without any leakage of radiation [64]. The authentic BIC phenomenon exists only in infinitely extended structures at least in one dimension. On the contrary, BIC phenomenon is forbidden in a single particle system with nonzero finite permittivity and

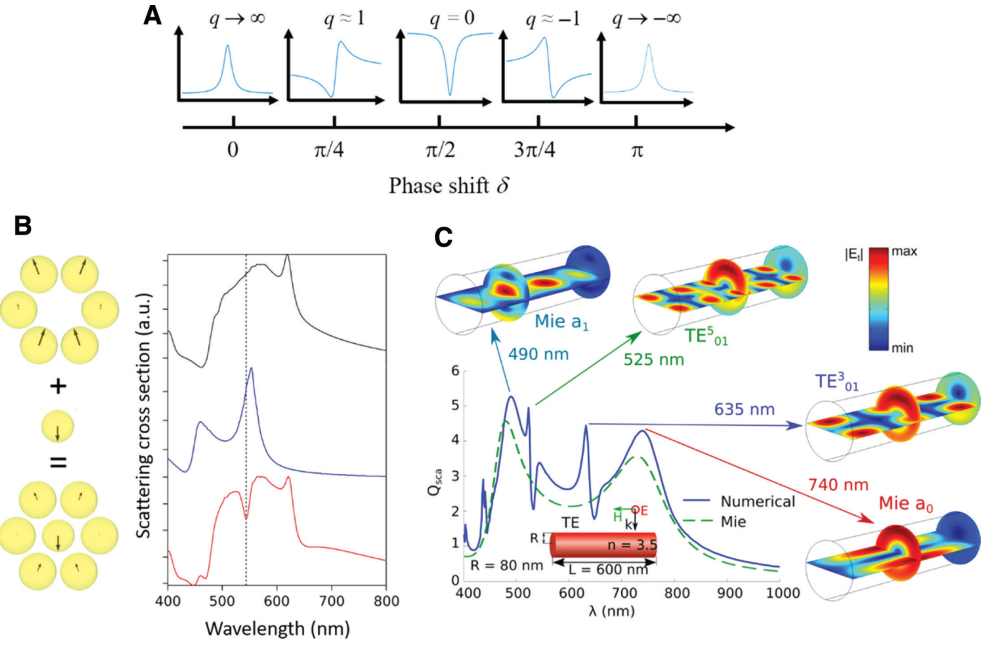

Figure 5: The concept and the application of Fano resonance.
(A) Variation of Fano line-shapes with respect to δ and q. (B) Fano resonance (red) produced by the destructive interference between single particle (blue) and outer ring (black) in Si-heptamer. (C) Fano resonance in a single nanorod, produced by the combination of Mie modes (continuum-like) and FP modes (discrete states-like). Adapted with permission from Refs. [57, 58].

permeability, arising from the continuity condition at the boundary of particle [65]. For a finite number of particles (e.g. 1D chain), quasi-BIC with a finite but ultrahigh Q-factor appears as an approximation of authentic BIC in infinite structures [66]. Although photonic BIC and quasi-BIC have already been demonstrated in many extended structures, like photonic crystal slabs [67–69], metasurfaces [70, 71], and 2D nanowire array [72, 73], we also notice an emerging type of quasi-BIC analogue or the so-called "supercavity mode" mediated by a single Mie resonator (Figure 6A) [74–76]. According to the Friedrich-Wintgen scenario [64, 77], while two resonant modes, Mie-like mode and FP-like mode, are excited in a single high-index Mie nanocylinder and strongly coupled to the same radiation channel (radiation continuum), while the aspect ratio of Mie resonator (r/l) is tuned continuously, one can find a totally suppressed radiation channel via destructive interference between Mie mode and FP mode. Therefore, quasi-BIC can be regarded as a singularity of the Fano parameter ($q \to \infty$, radiation continuum is uncoupled from external excitation), resulting in the occurrence of an ultrahigh Q-value mode (the so-called supercavity mode) in the scattering spectrum. Interestingly, the anticrossing behavior (large red circle in Figure 6B) indicates the strong coupling between Mie-like mode ($TE_{1,1,0}$, mode A in Figure 6B, C) and FP-like mode ($TM_{1,1,1}$, mode B in Figure 6B, C), resulting from their same azimuthal mode symmetry and the inversion symmetry of Mie resonator. For quasi-BIC of $TM_{1,1,1}$ (Figure 6C), magnetic quadrupole (MQ in Figure 6D) contributes dominantly to the total far-field radiation pattern and the radiation channel. Multipole expansion enables clear explanation and sufficient details of phase and vectorial distribution in each multipole term [78–80]. Additionally, a fast-changing far-field pattern with respect to the aspect ratio of Mie resonator corresponds to the contributions from other resonant modes. Note that such quasi-BIC phenomenon is not only limited in 3D single nanocylinder but has also be reported in single microcavity [81], few nanodisks [66], and nanowires [82]. Very recently, a general comparison for evaluation of Q-factor of single subwavelength dielectric nanocavity has been reported elsewhere [80].

3 Multipole and multimode engineering in meta-lattices and meta-assembly

To realize multipole engineering in planar optics, an array or assembly of nanostructures is frequently used. In this section, we physically focus on multimode engineering-based collective coupling and resonance in 2D periodic or aperiodic metastructures. As a well-known example, the

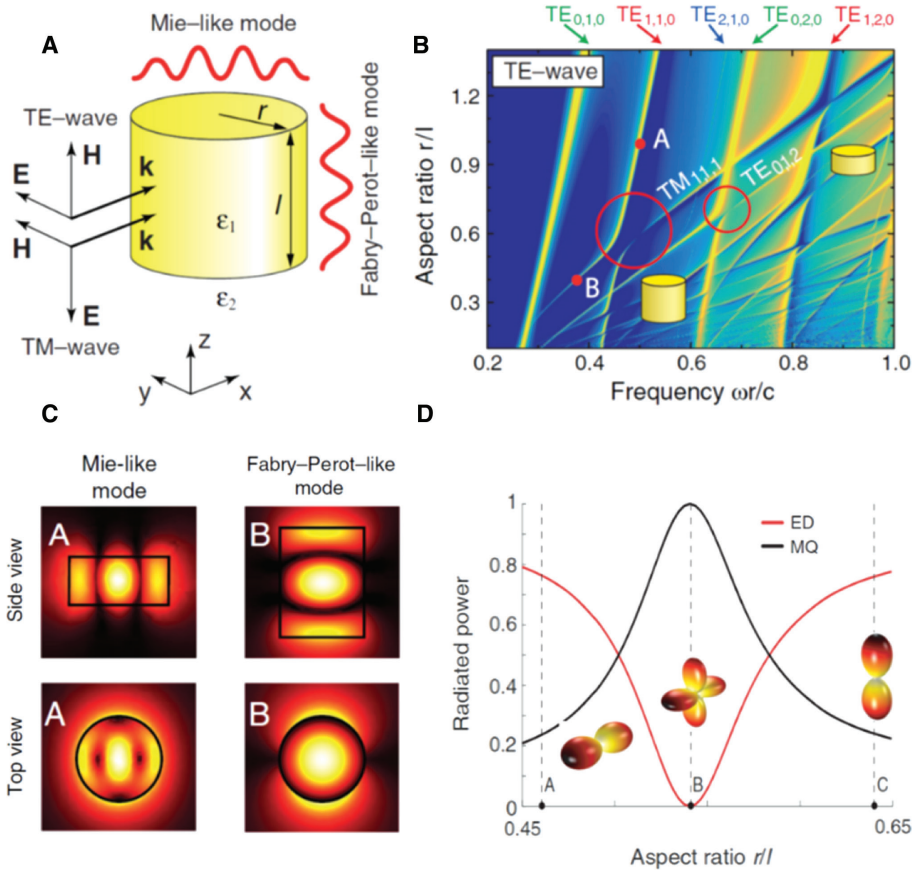

Figure 6: Quasi-BIC mode in a single Mie resonator.
(A) The Mie-like mode and FP-like mode generated in high-index Mie resonator. (B) The map of scattering cross-section with respect to aspect ratio (r/l) of Mie resonator. Points A and B are chosen as Mie-like mode and FP-like mode, respectively. (C) E-field distributions at A and B. (D) Multimode expansion of $TM_{1,1,1}$ mode. In comparison, the far-field radiation patterns (insets) are shown at points a, b, c. Adapted with permission from Ref. [74].

phase-gradient metasurface is typically defined as an interface evaluated by effective permittivity and permeability, leading to discontinuity in a certain direction and enforcing an abrupt change in both the amplitude and phase of the impinging wavefront. Several types of phase-gradient dielectric metasurface, like high-contrast array, Pancharatnam-Berry phase-based metasurface, and dispersion-engineered metasurface, are usually explained by phase jumps, impedance matching, and generalized refraction law, which present less or ambiguous associations with multipole and multimode engineering exhibited in Mie resonant metastructures, and readers may find comprehensive reviews elsewhere [83–88]. To distinguish from the above metasurface and clearly indicate the role of multimode engineering in periodic and aperiodic configurations, here, we use "meta-lattices" and "meta-assembly" to describe such structures highlighting the multipolar and multimodal property via collective coupling and resonances. Although single meta-atom and meta-molecule provide an insightful interpretation of fundamental light-matter interactions in nanoscale, low scattering efficiency of a single structure is incapable in nanostructure-array-based practical applications. More seriously, the open cavity-like Mie resonator (unavoidable radiation loss) is restricted in obtaining high-quality factor and sufficient spectral resolution at resonance. Therefore, Mie resonant meta-lattices and meta-assembly exhibit not only the powerful potential of applications but also some novel physical phenomena that disappear in a single metastructure (such as coupled dipole resonance, surface lattice resonance).

3.1 Collective coupling effect in Mie resonant meta-lattices

In Mie resonant meta-lattices with subwavelength-sized period, the collective coupling effect is ubiquitous and sometimes manifested as period dependence while

diffraction modes are lacking. Many have papers reported period dependence in dielectric nanoarray in 1D and 2D. The introduction of period is not a simple expansion and superposition of single meta-atom or meta-molecule; instead, weak near-field coupling may change the collective electromagnetic response like effective permittivity and permeability. Effective medium theory enables to quantitatively analyze such collective effect; however, scattering matrix of collective mode is nontrivial to obtain from the arbitrary geometry of resonators array in metafilm. Several numerical methods, like finite elements method and finite-difference time-domain, are employed to evaluate the spectral responses of reflection, transmission, and absorption. As shown in Figure 7A, Lorentzian oscillator-like Si nanocubes induce the abrupt phase change of reflected wave at the resonant wavelength (the so-called backscattering property in Mie scattering) [89, 93]; two main peaks in visible wavelengths originate from ED and MD resonances. Strong period dependence existed in the array of Si nanocubes, indicating the role of interparticle coupling in meta-lattices (Figure 7A, bottom). Such period dependence is feasible to manipulate structural color generation by using dielectric meta-lattices, resulting in controllable color saturation (peak intensity) but maintaining color hue (peak wavelength). Additionally, Si oxidation enables further manipulation of structural color generation (Figure 7B, top) [90]. Si nanocube meta-lattices are oxidized by thermal annealing at a high-temperature oxygen atmosphere, encapsulated by a SiO_2 cover layer. The high permittivity contrast ensures drastic change in backscattering spectra, such as blue-shift color hue and gradually decreased color saturation, which can be observed with respect to annealing time; the results demonstrated remarkable color tunability and the functionality of invisible ink (Figure 7B, bottom). Besides oxidation-based spectral tunability, flexible substrate supporting hexagonal Si nanocylinder meta-lattices can be

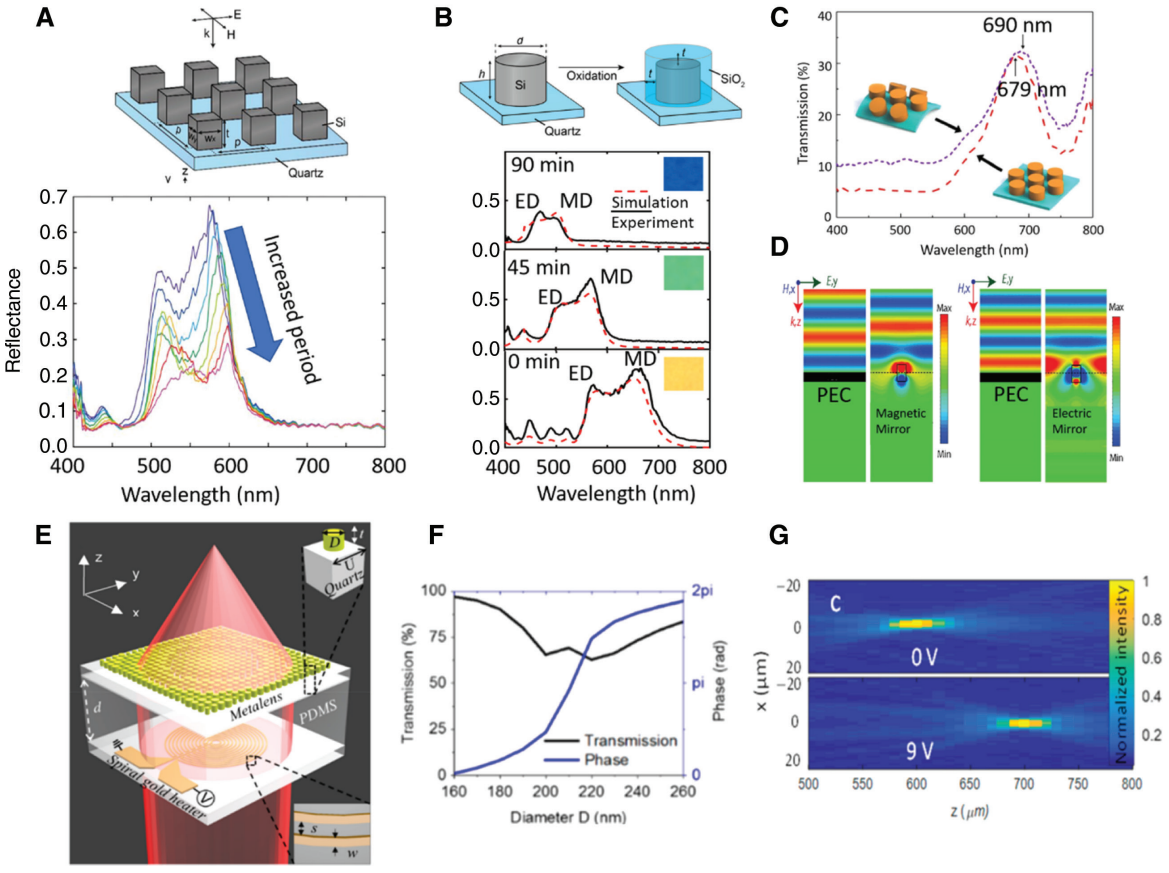

Figure 7: Collective coupling effect.
(A) Periodic Si nanocube array on a quartz substrate, and the reflection spectra with respect to period. (B) The optical property of oxidized Si nanocylinder array and the reflection spectra with respect to annealing time. (C) The reconfigurability of polymer-based flexible Si meta-lattices. (D) All dielectric meta-lattices mediated magnetic mirror (left) and electric mirror (right). (E–G) Thermal optic modulation-based varifocal Huygens metalens (E), 2π phase coverage and transmission efficiency with respect to nanodisk diameter (F), and the varifocal performance of metalens under the applied voltage in gold heater (0–9 V) (G). Adapted with permission from Refs. [89–92].

utilized as reconfigurable matastructures for sensing applications [91]. Polyethylene (PE) terephthalate-based flexible substrate displays sensitive response to externally applied force; a mechanical sensor is demonstrated by measuring the peak shift at MD resonance in transmission spectra, due to the deformation of meta-lattice-induced interparticle coupling (separation between hexagonal lattices is changed) (Figure 7C). Multiphysical field-mediated external modulation or tunability is not limited in oxidation and mechanical effect, but also by thermal-optical effect [94], electric-optical effect [95], and phase-change materials [96], to name a few.

In Section 2, single meta-atom-mediated HD is introduced as the combination of in-phase orthogonal ED and MD, which is featured by phase symmetry-based unidirectional emission. Similarly, dielectric perfect reflector [92, 97, 98] and transmitted Huygens surface (HS) [99–101] are proposed as phase-controlled metadevices to steer reflection/transmission, which are usually designed by periodic dielectric meta-lattices. The existence of ED and MD provides the possibility to control electric and magnetic resonances, respectively [92]. For magnetic perfect reflector (left in Figure 7D), near-zero phase change from incident excitation can be observed by the E-field profile of reflection, accompanying with the remarkable E-field enhancement at the interface of structure. On the contrary, for electric perfect reflector (right in Figure 7D), π-phase change and cancelled-out E-field are observed at the interface. Note that the magnetic perfect reflector is not limited in MD, but also in EQ and other high-order multipolar resonances, due to the same phase symmetry (parity) [102]. Magnetic dielectric perfect reflector is promising in near-field applications like Raman spectroscopy and fluorescence enhancement. One must also notice the importance of impedance matching in near-unity reflection/transmission meta-lattices, formulating into effective electric and magnetic polarizabilities in metastructures, which is related to interparticle coupling of meta-lattices [103], and the optical constant of substrate/superstrate [104]. For full 2π phase coverage modulation, transmitted HS (all-dielectric) can be regarded as the combination of orthogonally arranged ED and MD resonances. While ED and MD resonances are frequency-overlapped, a full 2π phase coverage is obtained. As one practical structure of HS, a Si nanodisk array ensures polarization-insensitive high transmittance at telecommunication wavelength [99, 105, 106]. At optical frequency, such all-dielectric HS provides a platform for low-loss, highly efficient, and full phase coverage modulation, which is promising for imaging applications like metalens [107–111] and holography [112–114]. As shown in Figure 7E, a thermal optic modulation-based varifocal Huygens metalens is demonstrated. The whole device is composed of the all-dielectric HS (top, metalens part) and the 700-μm-thick polydimethylsiloxane (PDMS) slab loaded by gold heater (bottom, thermal-optic part). For metalens part, the diameter (D)-variable Si nanodisk array (160–260 nm in Figure 7F) is carefully designed for high focusing efficiency and guarantees 2π phase coverage at a specific wavelength (fulfilling Kerker condition for a certain diameter; Figure 7F). For the thermal-optic part, a voltage-controlled gold heater that generates Ohmic heat is responsible for thermal-optic modulation of PDMS (temperature-dependent refractive index), imparting the varifocal functionality to Huygens metalens (Figure 7G). Aside from varifocal functionality, near-unity numerical aperture [107], a narrow field, and a wide field of view [108–111] are also demonstrated in Huygens metalens.

3.2 Surface lattice resonance in Mie resonant meta-lattices

In Section 3.1, we introduced the collective coupling in subwavelength-sized meta-lattices, which displays weak interparticle coupling in periodic structures and recognizable dipole or multipole resonances originating from a single meta-atom or meta-molecule. While the period of meta-lattices is comparable with wavelength, coupled resonances in meta-lattices may induce a diffraction mode (Rayleigh anomaly) in the surrounding [115, 116] and guided mode in adjacent waveguide [117], inducing an intermodal coupling between diffraction modes and multipole modes (supported by meta-atom or meta-molecule). Interestingly, the coupling between the ED, MD, and lattice modes enables two new modes termed as ED-LR and MD-LR, respectively, which can be separately controlled by different dimensions of periodicity in lattices (P_x and P_y). As an expansion of HS, ED-LR is spectrally overlapped with MD resonance, resulting in the occurrence of resonant lattice Kerker effect [93, 118, 119]. The surface lattice mode can also facilitate obtaining a high Q-factor in metastructures [117, 120, 121]. As shown in Figure 8A, a Si cylinder meta-lattice (a one unit cell with 100 nm height and variable diameters [d_a] is shown in the inset of Figure 8A) is embedded into fused silica (extended structures, not waveguide) [117]. In contrast to Fano resonance-based surface lattice resonance in plasmonic structures, the collective resonant modes [103] here are formed by strong coupling between single particle dipole modes (ED, MD) and surface lattice modes (Rayleigh anomaly), revealing a large detuning in mode coupling (Figure 8B). Both sharp peaks in the range of 600–650 nm correspond ED-LR

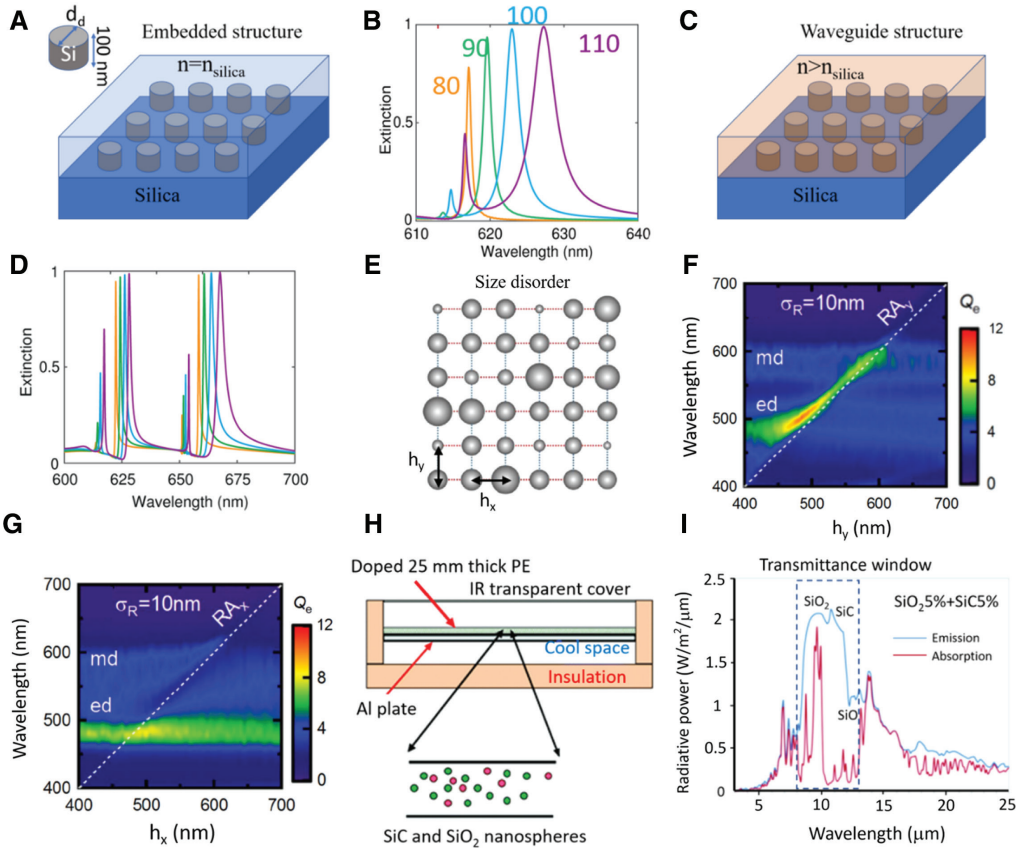

Figure 8: Multimode coupling in meta-lattices and meta-assembly.
Si cylinders meta-lattice embedded into fused silica (A) and in waveguide (C), the corresponding extinction spectra of surface lattice modes in fused silica (B) and in waveguide (D) with respect to d_d (color lines in (B, D), the value of dd). (E–G) Size disordered Si meta-assembly (E) and extinction map of ED and MD modes at σ_R=10 nm with respect to h_x (F) and h_y (G), respectively. Q_e is extinction efficiency. (H) Schematic of passive cooling system composed by SiC and SiO_2 nanocomposite. (I) The cooling performance of such SiC and SiO_2 nanocomposite. Adapted with permission from Refs. [117, 122, 123].

and MD-LR, respectively. The red shift of peak positions is observed with respect to the increasing d_d (numbers are labeled in Figure 8B). The sharp peaks are favorable for field enhancement and high Q-factor applications. In waveguide configuration (Figure 8C), a finite-thick high-index layer is utilized as core layer (brown layer, and the top cladding is air) in slab waveguide, in order to support quasi-guided modes. ED (MD) mode is efficiently coupled to transverse electric (TE) mode transverse magnetic (TM) mode, due to the symmetry of mode profiles. Again, the strong coupling between single particle dipole modes and quasi-guided modes (fundamental modes and high-order modes) leads to a large detuning and ultranarrow lattice-based resonant peaks (Figure 8D). Two pairs of peaks in the range of 600–700 nm are TE0(TM0)-LR and TE1(TM1)-LR modes (high-order modes), respectively. The quasi-guided modes provide strongly confined mode profiles, leading to a further field enhancement and higher Q-factor with respect to ED-LR and MD-LR. Instead of dipole mode, such mode coupling can also occur between Mie resonance-based AM and lattice modes; an ultrahigh Q-factor (~10^6) is numerally demonstrated in Si hollow nanocuboids meta-lattices [124].

3.3 Light-matter interactions in meta-assembly

In contrast to ordered photonic arrays, disordered photonic structures are more generalized photonic structures in meta-assembly. Understanding the evolution and differences between ordered and disordered meta-structures is crucial in nanotechnology. As shown in Figure 8E, size-disordered meta-assembly is composed of Si nanospherical arrays with unequal radii [122]; here, σ_R is the radius deviations in assembly and the radius of Si nanospheres (R) is randomly changed by a uniform distribution: $R_0 - \sigma_R < R < R_0 + \sigma_R$, where R_0 is the radius of ordered Si

nanospheres. In both ED coupling (with respect to h_y; Figure 8F) and MD coupling (with respect to h_x; Figure 8G), MD modes are suppressed while s_R is increased, indicating the radius-sensitive MD modes in size-disordered meta-assembly. In contrast, ED modes are more stable with respect to σ_R; counterintuitively, lattice mode coupling-like ED-LR modes can also be observed in such disordered structures. Other disordered meta-assembly-like position disorder (in two-dimension) and quasi-random structures [122] are also intriguing in controlling collective resonances and inducing phase transitions [125].

Randomized micro/nanoparticle assemblies are feasible for large-area and cost-effective applications. Multi-scattering-induced broadband absorption is favorable for passive cooling [126] and photothermal conversion [127, 128]. As the requirement of the passive cooling, expectedly, near-unity thermal emission should only appear within 8–13 μm, in order to cover the atmospheric transmitted window and use ultracold universe as a heat sink. Meanwhile, daytime passive cooling requires the suppression of absorption in visible wavelengths. To this end, randomized SiC and SiO-overcoated SiO_2 (to further broaden absorption band) nanospheres are mixed and doped into PE thin film (Figure 8H) [123]. The emission spectrum is effectively expanded by SiC and SiO_2 nanocomposite and lies within atmospheric transmittance window, due to their strong surface phonon resonances (Figure 8I; SiC: 10.5–13 μm, SiO_2 + SiO: 8–13 μm). The cooling performance can be evaluated from the power difference between emission and absorption.

4 Multimode engineering in achiral and chiral metastructures

4.1 Achiral dielectric metastructures

Generally, chiral geometry is the structure lacking reflection and inversion symmetry. A chiral object and its mirror image are usually called “left-handed” and “right-handed” enantiomers, due to a very familiar example of our own hands. In biomolecules, S-enantiomer and R-enantiomer may show different chemical properties (e.g. in some drugs, one enantiomer is active, the other is inactive or adverse), which can be effectively distinguished by CDC spectroscopy. However, only a very small dissymmetry factor (g), which is a parameter to evaluate the strength of chiral effect, can be observed in molecules solution (typical value: $10^{-3} - 10^{-2}$[129]) and most of molecules show resonant peaks in ultraviolet (UV) wavelength. Thanks to field enhancement and confinement by nanostructures, plasmonic and dielectric are suitable for visible-light chiral enhancement and promising in chiral sensing and separation, chirality sensitive photochemistry, and the growth of chiral crystal. To analyze chiral response in a local area, the optical density of chirality, $C = -\frac{\omega}{2c^2}\mathrm{Im}(\mathbf{E}^* \cdot \mathbf{H})$, is usually employed, where c and ω are the speed and angular frequency of incident light, respectively. **E** and **H** are localized electric and magnetic fields. Described by this equation, several design rules enabling the chiral enhancing and sensing are concluded in the following: (1) spectrally overlapped, (2) parallelly overlapped, and (3) $\pi/2$ out of phase between **E** and **H** fields in the near-field region. Based on three design rules, many achiral dielectric structures have been proposed to manipulate localized electromagnetic fields (**E**, **H**) by multimode engineering (the interaction between CD mode and multipole modes), which give an identical response to two enantiomers (R and S) under circularly polarized light (CPL; including left circularly polarized light [LCP] and right circularly polarized light [RCP]) and improve g-factor in chiral photoreactions. In contrast, chiral metastructures usually generate so strong chiral signals (CDC and g) that overwhelm the weak intrinsic signals from molecules, interfering chiral molecule sensing and analysis.

For a Si sphere, as shown in Figure 9A [130], observable CDC enhancement (C/C_{CPL}) is obtained from each Mie resonant multipolar peak, especially at high-order magnetic multipolar peaks (magnetic octupole [MO], magnetic 16-pole [MS], magnetic 32-pole [MT] in the CDC enhancement, Figure 9B), due to the strongly enhanced and localized **E** and **H** hotspots matching the vibrational band of typical chiral molecules nearby [134]. Additionally, the Si sphere can be used as an optical antenna to tailor the far-field emission from chiral quantum emitters (point dipole source composed of ED and MD modes); in contrast, using the plasmonic counterpart can only obtain almost achiral scattered fields due to the excitation of dominant ED moment [135]. A Si cube-dimer [136] is practical to further enhance chiral hotspots via spectrally and parallelly overlapped **E** and **H** fields at the subwavelength-sized gap, which can be interpreted as the superposition of hotspot by orthogonal linear polarizations of incident light. Interestingly, in Si cylinder-dimer, the net chiral density and flux in far-field can be observed even in linear polarized excitation (Figure 9C) [131]. Because linearly polarized light is equivalently decomposed to LCP and RCP, but undergo different dissipation induced by dimer axis for LCP and RCP, the result is an observable chiral signal-like chiral density in near-field and the third Stokes parameter

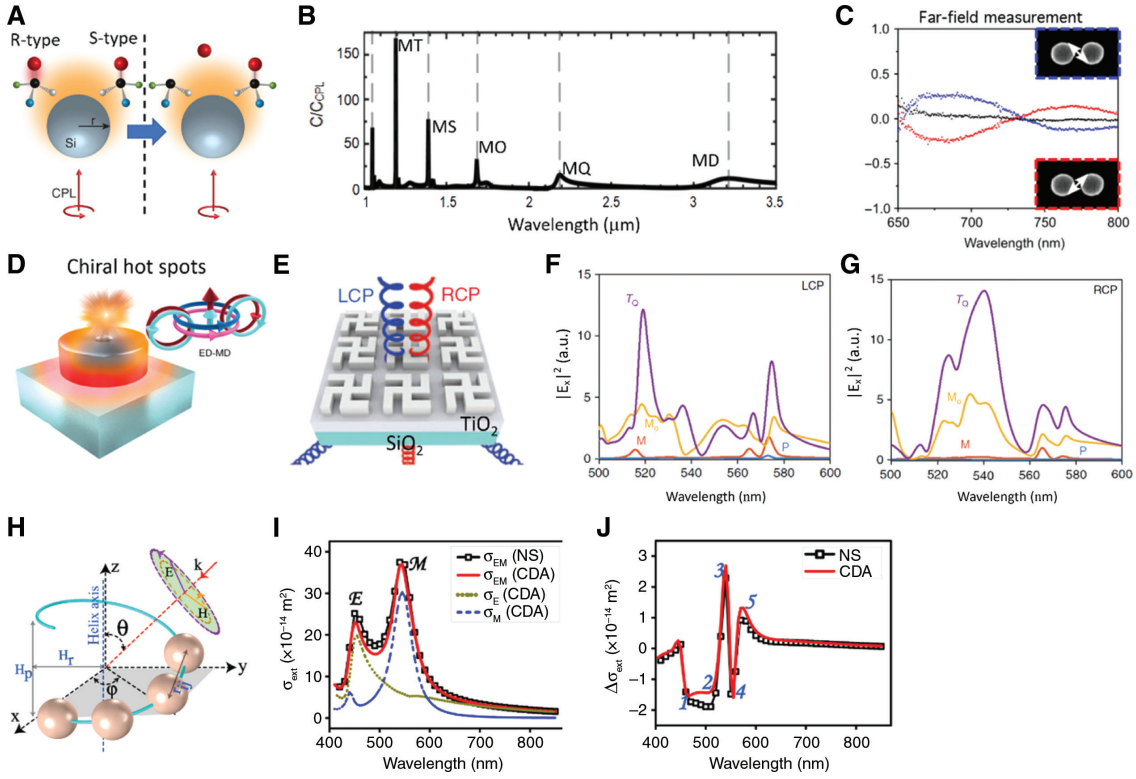

Figure 9: Multimode engineering in achiral and chiral metastructures.
(A) Achiral Si sphere for chiral sensing and separation; R-type and S-type denote R-enantiomer and S-enantiomer of chiral molecules, respectively. (B) Chiral enhancement mainly induced by magnetic multipole modes. (C) Si-dimer shows chiral density even in linear polarized excitation. (D) Chiral hotspots generated by holey Si nanodisk and overlapped ED and MD modes. (E–G) TiO_2-based chiral gammadion array for near-unity CDC. The multimodal expansion for LCP (F) and RCP (G), respectively. (H, I) Helically positioned Si chiral oligomer for chiral enhancement. Multipolar expansion used in the extinction spectra (I) and in the CDC spectra (J). NS and CDA denote numerical simulation and coupled dipole approximation, respectively. Adapted with permission from Refs. [27, 130–133].

(S3) in far-field. For near-UV enhancement, TiO_2-dimer is suitable for enhanced chiral sensing, due to the optical constant of material [137].

Achiral dielectric metasurfaces are widely used for the control of transmitted chiral spectra, due to the advantages of low loss, low heat generation, and high Q-factors [132]. Also, ordered array and collective response are indispensable for large-area chiral sensing and separation [132, 138–140]. Inspired by Si-dimers, holey Si nanodisk metasurface [132] effectively generates parallel and $\pi/2$ out-of-phase **E** and **H** fields, producing a superchiral field at the center of the a holey nanodisk (Figure 9D). According to the duality principle in classical electromagnetics, the direction of **E** and **H** fields of the ED mode is parallel with the corresponding **H** and **E** fields of MD mode, which guarantees the parallelly overlapped **E** and **H** fields as the aforementioned design rules for chiral nanostructures. Other design rules, like the spectrally overlapped and the $\pi/2$ out-of-phase **E** and **H** fields, are equivalent to the well-known Kerker condition. Note that the $\pi/2$ out-of-phase **E** and **H** fields are naturally fulfilled from incident plane wave (according to Maxwell's equations), implying the requirement of in-phase ED and MD modes in holey nanodisk metasurface. High transmission efficiency is also guaranteed in such all-dielectric metastructures.

4.2 Chiral dielectric metastructures

Artificially engineered chiral metastructures enable to further improve the CDC and *g*-factor of chiral response, which are promising for chiral optical devices such as polarization-resolved imaging and detection [141], reconfigurable chiral devices [142], and enhanced chiral sensing [143]. The lossless dielectric metastructures show multipolar excitation [27] and high efficiency chiral signal transmission [144, 145] with respect to their plasmonic counterpart. Planar chiral metastructures are widely applied for their relatively simple fabrication process and high compatibility in nanophotonics. As shown in Figure 9E, TiO_2-based

gammadion array metastructures are deposited on SiO_2 substrate [27]. Near-unity CDC is shown in transmitted spectrum at 540 nm for wavelength-sized metastructures (periodicity: 500 nm), which can be attributed to zero-order diffraction mode (transmission) under normally incident CPL. To clarify multimodal contribution, the results of multipole expansion extracted from far-field radiations are shown in Figure 9F, G. For the case of LCP, two remarkable dips appear around 540 nm, generated from toroidal quadrupole mode (T_Q, purple) and MO mode (M_O, yellow) (Figure 9F). In contrast, the radiation peaks of T_Q and M_O are observed around 540 nm (Figure 9G). The results indicate the near-unity CDC obtained by broken symmetry in gammadion metastructures and the suppressed dipole modes (or low-order modes) by wavelength-sized periodicity. Besides gammadion shape, other asymmetrical planar metastructures [144, 145] also support the strong chiral signal and accompanying more physical effects like Fano resonance [146].

The dielectric chiral oligomer is another important type of dielectric chiral metastructure, which can be composed by the assembly of achiral nanoparticles [133, 136, 147] or chiral nanohelices [148]. Dielectric chiral oligomers are mainly based on scattering CDC in extinction spectra, instead of absorption-based plasmonic counterpart, avoiding the photothermal effect induced photo-destruction [129]. As shown in Figure 9H, a Si-tetramer is helically positioned with the equal interparticle spacing [133]. From the extinction spectra of Si-tetramer under z-direction incident RCP, ED mode (σ_E) and MD mode (σ_M) appear in the visible range (Figure 9I). The corresponding contributions from ED and MD are calculated from multipole expansion of CDC spectra (Figure 9J); peak 1 is a pure ED mode, while peaks 2–4 are mainly induced by MD mode. One should note that such enhanced chiral fields are usually well confined within Si particles (Mie resonators), which implies the insensitivity of interparticle spacing in dielectric oligomers, in contrast to their plasmonic counterpart [149].

5 Multimode engineering in hybrid metastructures

On one hand, high-index dielectric metastructures provide a powerful platform for obtaining multipolar responses of Mie resonances and enhanced electromagnetic fields in metastructures. On the other hand, energy transfer between Mie resonant mode and adjacent optical emitters or other types of resonant modes (quasiparticles) is confirmed via weak and strong mode coupling behaviors in hybrid metastructures like Mie excitons [150] and dielectric-plasmonic structures [151–153]. In this section, our discussions are concentrated on the light-matter interaction in Mie resonance-mediated hybrid metastructures.

5.1 Mie-plasmon modes in hybrid metastructures

In the application of Purcell enhancement, metal nanoparticle on a mirror (MNPoM) is a well-studied plasmonic metastructure [154–156], featured by the generation of gap-plasmon mode in a nm-sized gap layer. While the quantum emitters embedded nanogap shrinks from ~10 nm to ~1 nm, MNPoM undergoes an extremely sensitive change in coupling strength from weak coupling (Purcell enhancement) to strong coupling [157]. More severely, quantum effects like the electron tunneling and nonlocal screening are dominant in a subnanometer gap [158]. In contrast, low-loss Si nanoparticle on a mirror (SiNPoM) is promising in obtaining a gap-insensitively resonant peak position (Figure 10A [159]) while eliminating the nonradiative decay of metal nanoparticles [163]. In such Purcell enhancement configuration, a nano-sized gap layer is composed of a Si quantum dot (QD) monolayer, which are used not only as a phosphor but also as an accurately controlled spacer. The Mie-plasmonic hybrid mode is strongly enhanced and well confined in the gap under the oblique excitation (Figure 10A). Physically, the hybrid mode arises from the coupling between a perpendicularly orientated ED mode (out of plane) and its image dipole mode supported by an Au mirror, which ensure the gap (spacer)-insensitive property of scattering peaks (color lines in Figure 10B). Distinguished with MNPoM, SiNPoM enables gap-controlled coupling strength but almost stable peak positions. Additionally, ED mode and MD mode are together responsible for broadband scattering (Figure 10B). Note that the different coupling performances in low-order and high-order hybrid modes may induce plasmon-like mode and dielectric mode, respectively [164]. Such gap insensitivity and broadband emission are favorable for simplifying the design and fabrication of nanogap resonator.

Besides the assembly of nanogap resonator, the combination of plasmonic and dielectric nanocavity uncovers a rich physics and potential to tailor the multipolar scattering spectra of planar metastructures. In order to achieve ultrahigh-resolution meta-atom-based color printing, the key is to decrease the impact from interparticle coupling in densely arranged dielectric meta-atoms. As shown in visible reflection spectra (backscattering), multipolar

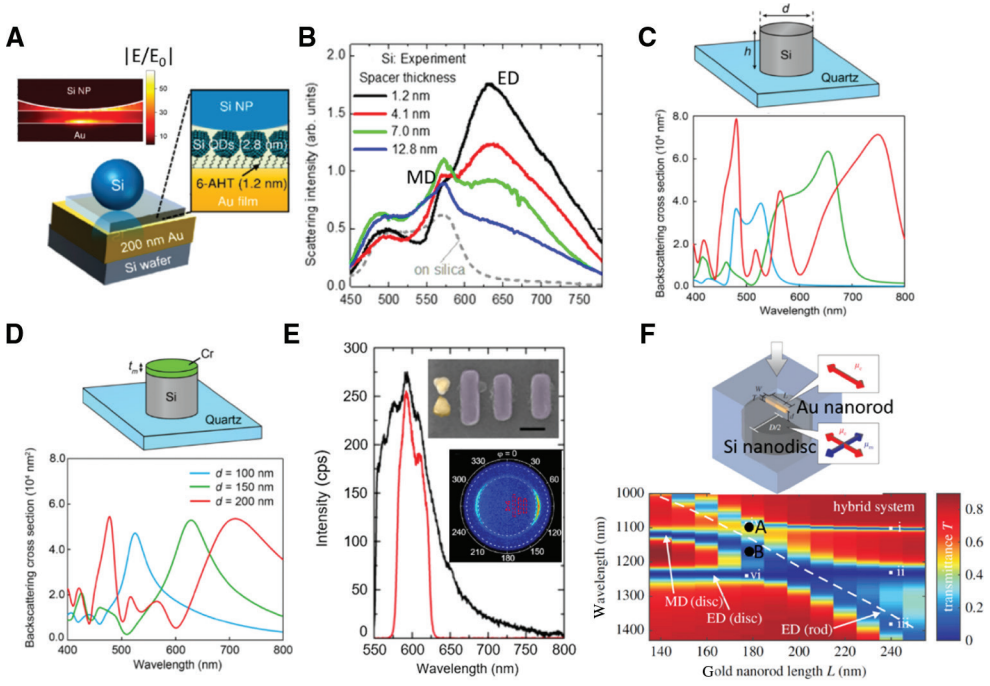

Figure 10: Mie-plasmon modes.
(A) In SiNPoM configuration, a monolayer of Si QDs (spacer) filled the gap between Si nanoparticle (Si NP) and Au mirror. The top inset shows the remarkable E-field enhancement. (B) The measured scattering spectra of SiNPoM with respect to spacer thickness. (C, D) The calculated backscattering spectra of single Si nanocylinder (C) and Cr-masked Si nanocylinder (D) on quartz with variable diameter (D). (E) Photoluminescence spectra of hybrid Au bowtie-Si Yagi-Uda nanoantennas (black). Red curve showed PL emission through a 600-nm band pass filter. Scanning electron microscopy image showed at the top inset; the scale bar is 100 nm. Measured directional emission is shown in a back focal image at the bottom inset. (F) Strong coupling phenomenon in Au nanorod-Si nanodisc hybrid system (orientations of dipole modes are shown in both parts). The transmittance map shows the crossing and anticrossing behavior for PED-MED coupling (b) and PED-MMD coupling (a), respectively. Adapted with permission from Refs. [159–162].

property of scattering can be observed from the Si nanocylinder array and further broadened spectra with respect to the increased diameter of Si nanocylinder, resulting in the degradation in the performance of color printing like color mixing (Figure 10C) [160]. In stark contrast, metal-masked Si Mie resonator is one feasible solution (Figure 10D); the addition of thin Cr layer (e.g. 30 nm) enables effective suppression of ED and MD peaks induced by Si nanocylinders. Importantly, such suppression is wavelength dependent and nonuniform for ED, MD, and high-order Mie peaks, generating brilliantly tunable reflection full colors with sufficient color saturation in ~μm² area.

Optical nanoantennas facilitate local control of intensity, polarization, and directionality of light [165]. Thanks to the excitation of localized plasmon, plasmonic antennas hold promise for obtaining the ultrasmall mode volume and high Purcell enhancement. However, unavoidable dissipation of metallic materials becomes a barrier for realizing highly efficient nanoantennas. Alternatively, dielectric-plasmonic hybrid nanoantennas may mitigate this situation [161, 166]; as shown in Figure 10E, high light collection and scattering efficiency are obtained by subwavelength-sized Au bowtie antennas, then the scattering light is coupled into Si Yagi-Uda antennas and the directional emission pattern is formed by asymmetrical shape of Si antennas (bottom inset in Figure 10E). Importantly, directionality is sensitive to the alignment between Au and Si antennas, which is useful for nanoscale positioning sensors. Aside from directional control, the research of hybrid nanoantennas is also active on nonlinear optics, especially for multiple harmonic generation [167, 168], due to the plasmon-enhanced conversion efficiency.

To investigate the strong mode coupling between plasmonic nanoantennas and Si nanodisc, a combination of Au nanorod and Si nanocavity is shown in Figure 10E; the entire metastructure is embedded into a homogenous dielectric medium (low index, $n = 1.45$ is chosen). Plasmonic ED (PED) mode is dominantly supported in a subwavelength-sized Au nanorod, and Mie resonance-based ED (MED) and MD (MMD) modes are supported by wavelength-comparable (λ/d_h, d_h is the diameter of nanodisc) Si nanodisc (transmittance map in Figure 10E)

[162]. The hybrid metastructure is used as a unit cell of meta-lattices, and the transmittance is shown for such meta-lattices with respect to Au nanorod length. Dipolar modes excited from Au nanorod and Si nanodisc are labeled in the transmittance map; interestingly, different mode coupling behaviors are found in PED-MED and PED-MMD. For PED-MED coupling (point B in the bottom part of Figure 10E), a resonance crossing is observed indicating the weak coupling between two modes. For PED-MMD coupling, the featured resonance anticrossing is observed, signifying the entry of strong coupling regime and hybridization of plasmonic-photonic modes (antibonding hybrid mode). Analyzed from the mode profiles at anticrossing and crossing points, the strong mode coupling phenomenon enhances the field distributions at the gap between Au rod and Si disc at two anticrossing points, inducing the pair of antibonding and bonding modes. On the contrary, approximate isolated resonant behaviors in Au rod and Si disc can be observed at the crossing point (PED-MED), implying relatively weak coupling between them.

5.2 Mie-exciton modes in hybrid metastructures

Recently, the resonant mode coupling phenomena between excitonic emitters and Mie resonator are numerically or experimentally demonstrated by observation of a large Rabi-splitting phenomenon in molecular *J* aggregate [169, 170] and transition-metal dichalcogenide (TMDC) materials [171–174] incorporated hybrid metastructures. *J* aggregate is well known for collective excitons featured by large oscillator strength and the ease of integration in organic-inorganic hybrid metastructures [175]. The hybridization and coupling of plasmon mode and molecular exciton mode in *J* aggregates (the so-called plexcitons) have been extensively reported [176–178]. In contrast to plasmonic system, the utilization of high-index Mie resonator not only decreases nonradiative decay but also generates unidirectional emission of hybrid modes, which is associated with the multipolar property of Mie scattering. One simple hybrid metastructure is Si-*J* aggregate core-shell nanoparticle [169]. Si core can be directly analyzed by multipolar expansion, extracting the contributions from ED, MD, EQ, and MQ modes (SiEDR, SiMDR, SiEQR, Sand iMQR, respectively, in Figure 11A). The dielectric function of the *J* aggregate shell is formulated by using a one-oscillator Lorentzian model,

$$\varepsilon_{ex}(\omega) = \varepsilon_{\infty} - \frac{f\omega_0^2}{\omega^2 - \omega_0^2 + i\omega\gamma_0} \tag{2}$$

Here, ε_{∞} is the dielectric constant at the frequency infinity, assuming equal value as the permittivity of the surrounding (e.g. water). ω_0, γ_0, f are the resonant frequency of exciton, the damping coefficient, and the

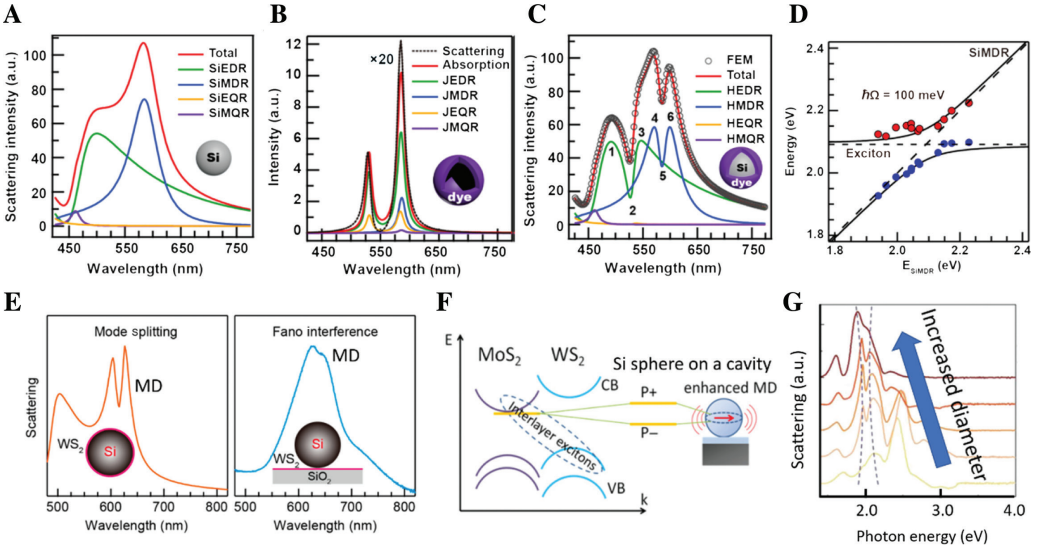

Figure 11: Mie-exciton modes.
(A–D) Strong mode coupling phenomenon is shown in Si-*J* aggregate core-shell nanoparticles. Scattering spectra of Si nanoparticle (A), absorption spectra of *J* aggregates, Scattering spectra of core-shell nanoparticle. Multipole expansion results are shown in (B–D). (E) Mode splitting between MD and exciton mode in Si core and monolayer WS_2 shell nanoparticle (left), and Fano resonance from Si nanoparticle on monolayer WS_2 flake. (F) Schematic of interlayer excitons-based strong coupling and mode splitting in WS_2/MoS_2 heterostructures. (G) Anti-crossing behavior observed in scattering spectra of Si nanoparticle-WS_2/MoS_2 hybrid system. Adapted with permission from Refs. [169, 172, 174].

oscillator strength in the *J*-aggregate, respectively. While ω_0 is carefully tuned to the same resonant frequency of SiMDR, two excitonic absorption peaks are observed in Figure 11B, due to the resonant property of the dielectric function $\varepsilon_{ex}(\omega)$ and the specified value of f and γ_0. Again, the absorption spectrum of *J* aggregate-shell can also be extracted into ED, MD, EQ, and MQ modes (JEDR, JMDR, JEQR, and JMQR in Figure 11B). The absorption peaks in *J* aggregate-shell correspond to scattering dips in hybrid metastructures (core shell). Interestingly, two scattering dips are mainly controlled by the resonant coupling of JEDR-SiMDR (HMDR in Figure 11C) and JEDR-SiEDR (HEDR in Figure 11C); moreover, two dips become deeper respect to the increasing *f* (Figure 11C). The strong coupling effect can be verified by the large Rabi-splitting (~100 meV) between high-energy branch and low-energy branch in the resonant peak map of SiMDR (Figure 11D). Note that the resonant peaks at both energy branches are unidirectional scattering modes, resulting from the Kerker condition in the strong mode coupling region of SiEDR, SiMDR, and excitonic modes.

As one promising candidate material in TMDCs, monolayer or multilayer WS_2 exhibits a large transition dipole of excitons. Similar to Si-*J* aggregate hybrid structures, the combination of Si nanoparticle and monolayer WS_2 enables the observation of mode splitting between Mie modes and exciton modes; moreover, the discovery of exotic optoelectronic properties of TMDCs is promising for applications of actively tunable devices [179–181]. In the Si core and monolayer WS_2 shell hybrid system, mode splitting phenomenon is obtained from resonant coupling between MD mode and excitonic mode (A-exciton) (left in Figure 11E) [172]. The high index of monolayer WS_2 enables the red-shift of MD mode in Si core, resulting in increased spectral overlap between two modes. However, mode splitting is lacking in absorption spectra, implying the weak coupling in this case. In comparison, Si nanoparticle on monolayer WS_2 flake reveals Fano-like line shape in scattering spectra (right in Figure 11E), indicating the smaller coupling strength between MD mode in Si nanoparticle and exciton mode in WS_2 flake [172]. Interestingly, both configurations exhibit directional scattering pattern transferred from MD mode. In WS_2/MoS_2 heterostructures, interlayer excitons may appear in such misaligned energy band structure (Figure 11F) [174], which can be confirmed by small red shift or blue shift with respect to pure monolayer or few-layer WS_2 and MoS_2. Using Si nanoparticle deposition on WS_2/MoS_2 heterostructure and a designed SiO_2/Si substrate, the hybrid system can be interpreted as a combination of the WS_2/MoS_2 heterostructures and the Mie-FP cavity (SiO_2/Si substrate) configuration. Strong coupling phenomena are observed by anticrossing behavior (MD mode and interlayer exciton mode) in such a hybrid system (Figure 11G). Note the FP cavity can further enhance MD mode in Si nanoparticle. Additionally, multilayer WS_2 can be regarded as an anisotropic high-index dielectric with excitonic resonance at a certain frequency [173]. In the high aspect ratio geometry of WS_2 nanodisk (excitonic Mie resonator), the dark mode-like AM can be excited and form a hybrid anapole-exciton polariton mode. Except the strong mode coupling phenomenon in Mie-TMDCs hybrid system, Si nanowire antenna enables the directional tailoring of radiation pattern in adjacent MoS_2 monolayer [182], resulting from the resonant coupling between exciton mode in MoS_2 and multipolar modes in Si nanowire.

6 Summary and outlook

The revisiting of century-old Mie scattering provides a powerful nanophotonic platform for many phenomena in metastructures. Multipole and multimode engineering manipulates mode interference in meta-atom or meta-molecule, collective resonance and lattice modes in meta-lattices and meta-assembly, spin angular momentum of light in achiral and chiral metastructures, and strong resonant coupling in hybrid systems, to name a few. High-index dielectric metastructures enable field enhancement and spatial confinement, a precondition of enhanced light-matter interaction in nanoscale. Low-loss dielectric materials definitely improve the efficiency of reflective/transmission or wavefront controlled metasurfaces. Optical magnetism like magnetic hotspot generation in the visible range is the unique advantage of dielectric metastructures for polarization and directionality associated applications.

Several emerging research subareas in dielectric metastructures are not discussed, due to the length and scope of this review. Here, we briefly mention achievements obtained in the following areas, which can be regarded as the outlook of dielectric metastructures. In nonlinear optics, nonlinear dielectric metasurfaces are feasible for efficient high-order harmonic generation and ultrafast control of optical switching [183, 184]. In spin-orbit interaction of light, meta-atoms or meta-molecules may realize the generation of optical vortex and transverse spin-Hall shift [185, 186]. In quantum optics, entangled photon states can be generated and manipulated in the platform of dielectric metastructures [187, 188]. In topological photonics, topological edge states in 1D chiral chains, 2D meta-lattices, 3D Si bianisotropic metacrystals

are recently demonstrated [29, 189, 190]. We anticipate that the rapid development in these emerging areas will become an impetus of nanophotonics in near future.

Acknowledgments: This work was supported by JSPS KAKENHI grant number JP19H02630 and the JSPS Core-to-Core Program, A. Advanced Research Networks (Advanced Nanophotonics in the Emerging Fields of Nano-imaging, Spectroscopy, Nonlinear Optics, Plasmonics/Metamaterials and Devices). T.L. and P.Y. were supported by the Institute of Fundamental and Frontier Sciences, University of Electronic Science and Technology of China. P.Y. was also supported by the China Postdoctoral Science Foundation (2019M663467, Funder Id: http://dx.doi.org/10.13039/501100002858).

References

[1] Mie G. Beiträge zur Optik trüber Medien, speziell kolloidaler Metallösungen. Ann Phys 1908;330:377–445.
[2] Horvath H. Gustav Mie and the scattering and absorption of light by particles: historic developments and basics. J Quant Spectrosc Radiat Transfer 2009;110:787–99.
[3] Johnson SG, Fan S, Villeneuve PR, Joannopoulos JD, Kolodziejski LA. Guided modes in photonic crystal slabs. Phys Rev B 1999;60:5751–8.
[4] Gramotnev DK, Bozhevolnyi SI. Plasmonics beyond the diffraction limit. Nat Photon 2010;4:83–91.
[5] Shalaev VM. Optical negative-index metamaterials. Nat Photon 2007;1:41–8.
[6] Jahani S, Jacob Z. All-dielectric metamaterials. Nat Nanotechnol 2016;11:23–36.
[7] Bohren CF, Huffman DR. Absorption and scattering of light by small particles. New York, John Wiley & Sons, 2008.
[8] Van de Hulst HC. Light scattering by small particles. New York, Courier Corporation, 1981.
[9] Kuznetsov AI, Miroshnichenko AE, Brongersma ML, Kivshar YS, Luk'yanchuk B. Optically resonant dielectric nanostructures. Science 2016;354:aag2472.
[10] Jackson JD. Classical electrodynamics. New York, John Wiley & Sons, 2007.
[11] Grahn P, Shevchenko A, Kaivola M. Electromagnetic multipole theory for optical nanomaterials. N J Phys 2012;14:093033.
[12] Radescu EE, Vaman G. Exact calculation of the angular momentum loss, recoil force, and radiation intensity for an arbitrary source in terms of electric, magnetic, and toroid multipoles. Phys Rev E Stat Nonlin Soft Matter Phys 2002;65:046609.
[13] Savinov V, Fedotov VA, Zheludev NI. Toroidal dipolar excitation and macroscopic electromagnetic properties of metamaterials. Phys Rev B 2014;89:205112.
[14] Staude I, Schilling J. Metamaterial-inspired silicon nanophotonics. Nat Photon 2017;11:274–84.
[15] Kruk S, Kivshar Y. Functional meta-optics and nanophotonics governed by Mie resonances. ACS Photon 2017;4:2638–49.
[16] Liu W, Kivshar YS. Generalized kerker effects in nanophotonics and meta-optics. Opt Express 2018;26:13085–105.
[17] Kuznetsov AI, Miroshnichenko AE, Fu YH, Zhang J, Luk'yanchuk B. Magnetic light. Sci Rep 2012;2:492.
[18] Fu YH, Kuznetsov AI, Miroshnichenko AE, Yu YF, Luk'yanchuk B. Directional visible light scattering by silicon nanoparticles. Nat Commun 2013;4:1527.
[19] Cao L, White JS, Park J-S, Schuller JA, Clemens BM, Brongersma ML. Engineering light absorption in semiconductor nanowire devices. Nat Mater 2009;8:643–7.
[20] Cao L, Fan P, Brongersma ML. Optical coupling of deep-subwavelength semiconductor nanowires. Nano Lett 2011;11:1463–8.
[21] Kim S-K, Day RW, Cahoon JF, et al. Tuning light absorption in core/shell silicon nanowire photovoltaic devices through morphological design. Nano Lett 2012;12:4971–6.
[22] Huang L, Yu Y, Cao L. General modal properties of optical resonances in subwavelength nonspherical dielectric structures. Nano Lett 2013;13:3559–65.
[23] Liu W, Zhang J, Lei B, Hu H, Miroshnichenko AE. Invisible nanowires with interfering electric and toroidal dipoles. Opt Lett 2015;40:2293–6.
[24] Zywietz U, Evlyukhin AB, Reinhardt C, Chichkov BN. Laser printing of silicon nanoparticles with resonant optical electric and magnetic responses. Nat Commun 2014;5:3402.
[25] Brongersma ML, Cui Y, Fan S. Light management for photovoltaics using high-index nanostructures. Nat Mater 2014;13:451–60.
[26] Cao L, Fan P, Vasudev AP, et al. Semiconductor nanowire optical antenna solar absorbers. Nano Lett 2010;10:439–45.
[27] Zhu AY, Chen W T, Zaidi A, et al. Giant intrinsic chiro-optical activity in planar dielectric nanostructures. Light Sci Appl 2018;7:17158.
[28] Karakasoglu I, Xiao M, Fan S. Polarization control with dielectric helix metasurfaces and arrays. Opt Express 2018;26:21664–74.
[29] Slobozhanyuk A, Mousavi SH, Ni X, Smirnova D, Kivshar YS, Khanikaev AB. Three-dimensional all-dielectric photonic topological insulator. Nat Photonics 2017;11:130–6.
[30] Meinzer N, Barnes WL, Hooper IR. Plasmonic meta-atoms and metasurfaces. Nat Photonics 2014;8:889–98.
[31] Raab RE, De Lange OL. Multipole theory in electromagnetism: classical, quantum, and symmetry aspects, with applications. Oxford University Press on Demand, 2005.
[32] Picardi MF, Zayats AV, Rodríguez-Fortuño FJ. Janus and Huygens dipoles: near-field directionality beyond spin-momentum locking. Phys Rev Lett 2018;120:117402.
[33] Shamkhi HK, Baryshnikova KV, Sayanskiy A, et al. Transverse scattering and generalized Kerker effects in all-dielectric Mie-resonant metaoptics. Phys Rev Lett 2019;122:193905.
[34] Picardi MF, Neugebauer M, Eismann JS, et al. Experimental demonstration of linear and spinning Janus dipoles for polarisation- and wavelength-selective near-field coupling. Light Sci Appl 2019;8:52.
[35] Zhang Y, Yue P, Liu J-Y, Geng W, Bai Y-T, Liu S-D. Ideal magnetic dipole resonances with metal-dielectric-metal hybridized nanodisks. Opt Express 2019;27:16143.
[36] Lodahl P, Mahmoodian S, Stobbe S, et al. Chiral quantum optics. Nature 2017;541:473–80.
[37] Bliokh KY, Rodríguez-Fortuño FJ, Nori F, Zayats AV. Spin-orbit interactions of light. Nat Photonics 2015;9:796–808.

[38] Liu Y, Ke Y, Luo H, Wen S. Photonic Spin hall effect in metasurfaces: a brief review. Nanophotonics 2017;6:51–70.
[39] Savinov V, Papasimakis N, Tsai DP, Zheludev NI. Optical anapoles. Commun Phys 2019;2:69.
[40] Tuz VR, Khardikov VV, Kivshar YS. All-dielectric resonant metasurfaces with a strong toroidal response. ACS Photonics 2018;5:1871–6.
[41] Papasimakis N, Fedotov VA, Savinov V, Raybould TA, Zheludev NI. Electromagnetic toroidal excitations in matter and free space. Nat Mater 2016;15:263–71.
[42] Miroshnichenko AE, Evlyukhin AB, Yu YF, et al. Nonradiating anapole modes in dielectric nanoparticles. Nat Commun 2015;6:8069.
[43] Zhang G, Lan C, Gao R, Wen Y, Zhou J. Toroidal dipole resonances in all-dielectric oligomer metasurfaces. Adv Theory Simul 2019;2:1900123.
[44] Pavlov N, Stenishchev I, Ospanova A, Belov P, Kapitanova P, Basharin A. Toroidal dipole mode observation in situ. Phys Status Solidi B 2019;1900406.
[45] Yang Y, Zenin VA, Bozhevolnyi SI. Anapole-assisted strong field enhancement in individual all-dielectric nanostructures. ACS Photonics 2018;5:1960–6.
[46] Tian J, Luo H, Yang Y, et al. Active control of anapole states by structuring the phase-change alloy Ge2Sb2Te5. Nat Commun 2019;10:396.
[47] Koshelev K, Favraud G, Bogdanov A, Kivshar Y, Fratalocchi A. Nonradiating photonics with resonant dielectric nanostructures. Nanophotonics 2019;8:725–45.
[48] Yang Y, Bozhevolnyi SI. Nonradiating anapole states in nanophotonics: from fundamentals to applications. Nanotechnology 2019;30:204001.
[49] Li S-Q, Crozier KB. Origin of the Anapole condition as revealed by a simple expansion beyond the toroidal multipole. Phys Rev B 2018;97:245423.
[50] Wolf E, Habashy T. Invisible bodies and uniqueness of the inverse scattering problem. J Mod Opt 1993;40:785–92.
[51] Monticone F, Sounas D, Krasnok A, Alù A. Can a nonradiating mode be externally excited? Nonscattering states versus embedded eigenstates. ACS Photonics 2019;6:3108–14.
[52] Monticone F, Alù A. Embedded photonic eigenvalues in 3D nanostructures. Phys Rev Lett 2014;112:213903.
[53] Totero Gongora JS, Miroshnichenko AE, Kivshar YS, Fratalocchi A. Anapole nanolasers for mode-locking and ultrafast pulse generation. Nat Commun 2017;8:15535.
[54] Luk'yanchuk B, Paniagua-Domínguez R, Kuznetsov AI, Miroshnichenko AE, Kivshar YS. Suppression of scattering for small dielectric particles: anapole mode and invisibility. Philos Trans A Math Phys Eng Sci 2017;375:20160069.
[55] Limonov MF, Rybin MV, Poddubny AN, Kivshar YS. Fano resonances in photonics. Nat Photonics 2017;11:543–54.
[56] Khromova I, Sayanskiy A, Uryutin A, Evlyukhin AB. Polarity of the Fano resonance in the near-field magnetic-dipole response of a dielectric particle near a conductive surface: polarity of the Fano resonance in the near-field magnetic-dipole response of a dielectric particle near a conductive surface. Laser Photonics Rev 2018;12:1800037.
[57] Miroshnichenko AE, Kivshar YS. Fano resonances in all-dielectric oligomers. Nano Lett 2012;12:6459–63.
[58] Abujetas DR, Mandujano MAG, Méndez ER, Sánchez-Gil JA. High-contrast Fano resonances in single semiconductor nanorods. ACS Photonics 2017;4:1814–21.
[59] Chong KE, Hopkins B, Staude I, et al. Observation of Fano resonances in all-dielectric nanoparticle oligomers. Small 2014;10:1985–90.
[60] Fan P, Yu Z, Fan S, Brongersma ML. Optical Fano resonance of an individual semiconductor nanostructure. Nat Mater 2014;13:471–5.
[61] Chong KE, Orton HW, Staude I, et al. Refractive index sensing with Fano resonances in silicon oligomers. Philos Trans A Math Phys Eng Sci 2017;375:20160070.
[62] Lee E, Seo IC, Jeong HY, An S-C, Jun YC. Theoretical investigations on microwave Fano resonances in 3D-printable hollow dielectric resonators. Sci Rep 2017;7:16186.
[63] Yang Y, Kravchenko II, Briggs DP, Valentine J. All-dielectric metasurface analogue of electromagnetically induced transparency. Nat Commun 2014;5:5753.
[64] Hsu CW, Zhen B, Stone AD, Joannopoulos JD, Soljačić M. Bound states in the continuum. Nat Rev Mater 2016;1:16048.
[65] Silveirinha MG. Trapping light in open plasmonic nanostructures. Phys Rev A 2014;89:023813.
[66] Sadrieva ZF, Belyakov MA, Balezin MA, et al. Experimental observation of a symmetry-protected bound state in the continuum in a chain of dielectric disks. Phys Rev A 2019;99:053804.
[67] Lee J, Zhen B, Chua S-L, et al. Observation and differentiation of unique high-Q optical resonances near zero wave vector in macroscopic photonic crystal slabs. Phys Rev Lett 2012;109:067401.
[68] Zhen B, Hsu CW, Lu L, Stone AD, Soljačić M. Topological nature of optical bound states in the continuum. Phys Rev Lett 2014;113:257401.
[69] Hsu CW, Zhen B, Lee J, et al. Observation of trapped light within the radiation continuum. Nature 2013;499:188–91.
[70] Koshelev K, Lepeshov S, Liu M, Bogdanov A, Kivshar Y. Asymmetric metasurfaces with high-Q resonances governed by bound states in the continuum. Phys Rev Lett 2018;121:193903.
[71] Kodigala A, Lepetit T, Gu Q, Bahari B, Fainman Y, Kanté B. Lasing action from photonic bound states in continuum. Nature 2017;541:196–9.
[72] Bulgakov EN, Sadreev AF. Bloch bound states in the radiation continuum in a periodic array of dielectric rods. Phys Rev A 2014;90:053801.
[73] Doeleman HM, Monticone F, den Hollander W, Alù A, Koenderink AF. Experimental observation of a polarization vortex at an optical bound state in the continuum. Nat Photonics 2018;12:397–401.
[74] Bogdanov AA, Koshelev KL, Kapitanova PV, et al. Bound states in the continuum and Fano resonances in the strong mode coupling regime. Adv Photonics 2019;1:1.
[75] Rybin MV, Koshelev KL, Sadrieva ZF, et al. High-Q supercavity modes in subwavelength dielectric resonators. Phys Rev Lett 2017;119:243901.
[76] Gladyshev SA, Bogdanov AA, Kapitanova PV, et al. High-Q states and strong mode coupling in high-index dielectric resonators. J Phys Conf Series 2018;1124:051058.
[77] Friedrich H, Wintgen D. Interfering resonances and bound states in the continuum. Phys Rev A 1985;32:3231–42.
[78] Chen W, Chen Y, Liu W. Singularities and poincaré indices of electromagnetic multipoles. Phys Rev Lett 2019;122:153907.
[79] Sadrieva Z, Frizyuk K, Petrov M, Kivshar Y, Bogdanov A. Multipolar origin of bound states in the continuum. Phys Rev B 2019;100:115303.

[80] Huang L, Xu L, Rahmani M, Neshev D, Miroshnichenko AE. Pushing the limit of high-Q mode of a single subwavelength dielectric nanocavity. arXiv 1909, 01512.
[81] Wiersig J. Formation of long-lived, scarlike modes near avoided resonance crossings in optical microcavities. Phys Rev Lett 2006;97:253901.
[82] Song QH, Cao H. Improving optical confinement in nanostructures via external mode coupling. Phys Rev Lett 2010;105:053902.
[83] Genevet P, Capasso F, Aieta F, Khorasaninejad M, Devlin R. Recent advances in planar optics: from plasmonic to dielectric metasurfaces. Optica 2017;4:139–52.
[84] Xiao S, Wang J, Liu F, Zhang S, Yin X, Li J. Spin-dependent optics with metasurfaces. Nanophotonics 2017;6:215–34.
[85] Kamali SM, Arbabi E, Arbabi A, Faraon A. A review of dielectric optical metasurfaces for wavefront control. Nanophotonics 2018;7:1041–68.
[86] Hsiao H-H, Chu C H, Tsai DP. Fundamentals and applications of metasurfaces. Small Methods 2017;1:1600064.
[87] Qiao P, Yang W, Chang-Hasnain CJ. Recent advances in high-contrast metastructures, metasurfaces, and photonic crystals. Adv Opt Photonics 2018;10:180–245.
[88] Bukhari SS, Vardaxoglou J, Whittow W. A metasurfaces review: definitions and applications. Appl Sci 2019;9:2727.
[89] Nagasaki Y, Suzuki M, Takahara J. All-dielectric dual-color pixel with subwavelength resolution. Nano Lett 2017;17:7500–6.
[90] Nagasaki Y, Suzuki M, Hotta I, Takahara J. Control of Si-based all-dielectric printing color through oxidation. ACS Photonics 2018;5:1460–6.
[91] Zhang G, Lan C, Bian H, Gao R, Zhou J. Flexible, All-dielectric metasurface fabricated via nanosphere lithography and its applications in sensing. Opt Express 2017;25:22038.
[92] Moitra P, Slovick BA, li W, et al. Large-scale all-dielectric metamaterial perfect reflectors. ACS Photonics 2015;2:692–8.
[93] Babicheva VE, Moloney JV. Lattice effect influence on the electric and magnetic dipole resonance overlap in a disk array. Nanophotonics 2018;7:1663–8.
[94] Lewi T, Evans HA, Butakov NA, Schuller JA. Ultrawide thermo-optic tuning of PbTe meta-atoms. Nano Lett 2017;17:3940–5.
[95] Komar A, Fang Z, Bohn J, et al. Electrically tunable all-dielectric optical metasurfaces based on liquid crystals. Appl Phys Lett 2017;110:071109.
[96] Nagasaki Y, Kohno T, Bando K, Takase H, Fujita K, Takahara J. Adaptive printing using VO2 optical antennas with subwavelength resolution. Appl Phys Lett 2019;115:161105.
[97] Gui X, Jing X, Hong Z. Ultrabroadband perfect reflectors by all-dielectric single-layer super cell metamaterial. IEEE Photonic Tech Lett 2018;30:923–6.
[98] Ko YH, Magnusson R. Wideband dielectric metamaterial reflectors: Mie scattering or leaky Bloch mode resonance? Optica 2018;5:289–94.
[99] Decker M, Staude I, Falkner M, et al. High-efficiency dielectric Huygens' surfaces. Adv Opt Mater 2015;3:813–20.
[100] Terekhov PD, Babicheva VE, Baryshnikova KV, Shalin AS, Karabchevsky A, Evlyukhin AB. Multipole analysis of dielectric metasurfaces composed of nonspherical nanoparticles and lattice invisibility effect. Phys Rev B 2019;99:045424.
[101] Yang Q, Kruk S, Xu Y, et al. Mie-resonant membrane Huygens' metasurfaces. Adv Funct Mater 2019;30:1906851.
[102] Liu W. Generalized magnetic mirrors. Phys Rev Lett 2017;119:123902.
[103] Evlyukhin AB, Reinhardt C, Seidel A, Luk'yanchuk BS, Chichkov BN. Optical response features of Si-nanoparticle arrays. Phys Rev B 2010;82:045404.
[104] Butakov NA, Schuller JA. Designing multipolar resonances in dielectric metamaterials. Sci Rep 2016;6:38487.
[105] Chong KE, Wang L, Staude I, et al. Efficient polarization-insensitive complex wavefront control using Huygens' metasurfaces based on dielectric resonant meta-atoms. ACS Photonics 2016;3:514–9.
[106] Chong KE, Staude I, James A, et al. Polarization-independent silicon metadevices for efficient optical wavefront control. Nano Lett 2015;15:5369–74.
[107] Paniagua-Domínguez R, Yu YF, Khaidarov E, et al. A metalens with a near-unity numerical aperture. Nano Lett 2018;18:2124–32.
[108] Afridi A, Canet-Ferrer J, Philippet L, Osmond J, Berto P, Quidant R. Electrically driven varifocal silicon metalens. ACS Photonics 2018;5:4497–503.
[109] Arbabi A, Arbabi E, Kamali SM, Horie Y, Han S, Faraon A. Miniature optical planar camera based on a wide-angle metasurface doublet corrected for monochromatic aberrations. Nat Commun 2016;7:13682.
[110] Groever B, Chen WT, Capasso F. Meta-lens doublet in the visible region. Nano Lett 2017;17:4902–7.
[111] Engelberg J, Zhou C, Mazurski N, Bar-David J, Kristensen A, Levy U. Near-IR wide-field-of-view Huygens metalens for outdoor imaging applications. Nanophotonics 2019;9:361–70.
[112] Huang L, Zhang S, Zentgraf T. Metasurface holography: from fundamentals to applications. Nanophotonics 2018;7:1169–90.
[113] Zhao W, Jiang H, Liu B, et al. Dielectric Huygens' metasurface for high-efficiency hologram operating in transmission mode. Sci Rep 2016;6:30613.
[114] Wang L, Kruk S, Tang H, et al. Grayscale transparent metasurface holograms. Optica 2016;3:1504–5.
[115] Shi T, Wang Y, Deng Z, et al. All-dielectric kissing-dimer metagratings for asymmetric high diffraction. Adv Opt Mater 2019:1901389.
[116] Du J, Lin Z, Chui ST, et al. Optical beam steering based on the symmetry of resonant modes of nanoparticles. Phys Rev Lett 2011;106:203903.
[117] Castellanos GW, Bai P, Gómez Rivas J. Lattice resonances in dielectric metasurfaces. J Appl Phys 2019;125:213105.
[118] Babicheva VE, Evlyukhin AB. Resonant lattice Kerker effect in metasurfaces with electric and magnetic optical responses. Laser Photonics Rev 2017;11:1700132.
[119] Babicheva VE. Lattice effect in Mie-resonant dielectric nanoparticle array under oblique light incidence. MRS Commun 2018;8:1455–62.
[120] Wang X, Kogos L C, Paiella R. Giant distributed optical-field enhancements from Mie-resonant lattice surface modes in dielectric metasurfaces. OSA Continuum 2019;2:32–42.
[121] Tsoi S, Bezares FJ, Giles A, et al. Experimental demonstration of the optical lattice resonance in arrays of Si nanoresonators. Appl Phys Lett 2016;108:111101.
[122] Zakomirnyi VI, Karpov SV, Ågren H, Rasskazov IL. Collective lattice resonances in disordered and quasi-random all-dielectric metasurfaces. J Opt Soc Am B 2019;36:E21–9.

[123] Gentle AR, Smith GB. Radiative heat pumping from the earth using surface phonon resonant nanoparticles. Nano Lett 2010;10:373–9.
[124] Algorri JF, Zografopoulos DC, Ferraro A, García-Cámara B, Beccherelli R, Sánchez-Pena JM. Ultrahigh-quality factor resonant dielectric metasurfaces based on hollow nanocuboids. Opt Express 2019;27:6320–30.
[125] Rahimzadegan A, Arslan D, Suryadharma RNS, et al. Disorder-induced phase transitions in the transmission of dielectric metasurfaces. Phys Rev Lett 2019;122:015702.
[126] Zhai Y, Ma Y, David SN, et al. Scalable-manufactured randomized glass-polymer hybrid metamaterial for daytime radiative cooling. Science 2017;355:1062–6.
[127] Ishii S, Sugavaneshwar RP, Chen K, Dao TD, Nagao T. Solar water heating and vaporization with silicon nanoparticles at Mie resonances. Opt Mater Express 2016;6:640–8.
[128] Zograf GP, Petrov MI, Zuev DA, et al. Resonant nonplasmonic nanoparticles for efficient temperature-feedback optical heating. Nano Lett 2017;17:2945–52.
[129] Liu T, Besteiro LV, Liedl T, Correa-Duarte MA, Wang Z, Govorov AO. Chiral plasmonic nanocrystals for generation of hot electrons: toward polarization-sensitive photochemistry. Nano Lett 2019;19:1395–407.
[130] Ho C-S, Garcia-Etxarri A, Zhao Y, Dionne J. Enhancing enantioselective absorption using dielectric nanospheres. ACS Photonics 2017;4:197–203.
[131] Zhao X, Reinhard BM. Switchable chiroptical hot-spots in silicon nanodisk dimers. ACS Photonics 2019;6:1981–9.
[132] Mohammadi E, Tavakoli A, Dehkhoda P, et al. Accessible superchiral near-fields driven by tailored electric and magnetic resonances in all-dielectric nanostructures. ACS Photonics 2019;6:1939–46.
[133] Singh H J, Ghosh A. Chiral assemblies of achiral dielectric nanoparticles: semianalytical approach. J Phys Chem C 2018;122:20476–82.
[134] Stephens PJ, Devlin FJ, Pan J-J. The Determination of the absolute configurations of chiral molecules using vibrational circular dichroism (VCD) spectroscopy. Chirality 2008;20:643–63.
[135] Zambrana-Puyalto X, Bonod N. Tailoring the chirality of light emission with spherical Si-based antennas. Nanoscale 2016;8:10441–52.
[136] Ullah K, Garcia-Camara B, Habib M, et al. Chiral all-dielectric trimer nanoantenna. J Quant Spectrosc Radiat Transfer 2018;208:71–7.
[137] Yao K, Zheng Y. Near-ultraviolet dielectric metasurfaces: from surface-enhanced circular dichroism spectroscopy to polarization-preserving mirrors. J Phys Chem C 2019;123:11814–22.
[138] Graf F, Feis J, Garcia-Santiago X, Wegener M, Rockstuhl C, Fernandez-Corbaton I. Achiral, helicity preserving, and resonant structures for enhanced sensing of chiral molecules. ACS Photonics 2019;6:482–91.
[139] Solomon ML, Hu J, Lawrence M, García-Etxarri A, Dionne JA. Enantiospecific optical enhancement of chiral sensing and separation with dielectric metasurfaces. ACS Photonics 2019;6:43–9.
[140] Hu J, Lawrence M, Dionne JA. High quality factor dielectric metasurfaces for ultraviolet circular dichroism spectroscopy. ACS Photonics 2020;7:36–42.
[141] Ye W, Yuan X, Guo C, Zhang J, Yang B, Zhang S. Large chiroptical effects in planar chiral metamaterials. Phys Rev Applied 2017;7:054003.
[142] Lan X, Liu T, Wang Z, Govorov AO, Yan H, Liu Y. DNA-guided plasmonic helix with switchable chirality. J Am Chem Soc 2018;140:11763–70.
[143] Hentschel M, Schäferling M, Duan X, Giessen H, Liu N. Chiral plasmonics. Sci Adv 2017;3:e1602735.
[144] Ma Z, Li Y, Li Y, Gong Y, Maier SA, Hong M. All-dielectric planar chiral metasurface with gradient geometric phase. Opt Express 2018;26:6067.
[145] Hu J, Zhao X, Lin Y, et al. All-dielectric metasurface circular dichroism waveplate. Sci Rep 2017;7:41893.
[146] Wu C, Arju N, Kelp G, et al. Spectrally selective chiral silicon metasurfaces based on infrared Fano resonances. Nat Commun 2014;5:3892.
[147] Lin L, Lepeshov S, Krasnok A, et al. All-optical reconfigurable chiral meta-molecules. Mater Today 2019;25:10–20.
[148] Feng W, Kim J-Y, Wang X, et al. Assembly of mesoscale helices with near-unity enantiomeric excess and light-matter interactions for chiral semiconductors. Sci Adv 2017;3:e1601159.
[149] Nair G, Singh HJ, Paria D, Venkatapathi M, Ghosh A. Plasmonic interactions at close proximity in chiral geometries: route toward broadband chiroptical response and giant enantiomeric sensitivity. J Phys Chem C 2014;118:4991–7.
[150] Tserkezis C, Gonçalves PAD, Wolff C, Todisco F, Busch K, Mortensen NA. Mie excitons: understanding strong coupling in dielectric nanoparticles. Phys Rev B 2018;98:155439.
[151] Lee T, Jang J, Jeong H, Rho J. Plasmonic- and dielectric-based structural coloring: from fundamentals to practical applications. Nano Convergence 2018;5:1.
[152] Nishi H, Tatsuma T. Full-color scattering based on plasmon and Mie resonances of gold nanoparticles modulated by Fabry-Pérot interference for coloring and image projection. ACS Appl Nano Mater 2019;2:5071–8.
[153] Bian Y, Gong Q. Multilayer metal-dielectric planar waveguides for subwavelength guiding of long-range hybrid plasmon polaritons at 1550 Nm. J Opt 2014;16:015001.
[154] Mock JJ, Hill RT, Degiron A, Zauscher S, Chilkoti A, Smith DR. Distance-dependent plasmon resonant coupling between a gold nanoparticle and gold film. Nano Lett 2008;8:2245–52.
[155] Rose A, Hoang TB, McGuire F, et al. Control of radiative processes using tunable plasmonic nanopatch antennas. Nano Lett 2014;14:4797–802.
[156] Yashima S, Sugimoto H, Takashina H, Fujii M. Fluorescence enhancement and spectral shaping of silicon quantum dot monolayer by plasmonic gap resonances. J Phys Chem C 2016;120:28795–801.
[157] Chikkaraddy R, de Nijs B, Benz F, et al. Single-molecule strong coupling at room temperature in plasmonic nanocavities. Nature 2016;535:127–30.
[158] Zhu W, Esteban R, Borisov AG, et al. Quantum mechanical effects in plasmonic structures with subnanometre gaps. Nature Commun 2016;7:11495.
[159] Sugimoto H, Fujii M. Broadband dielectric-metal hybrid nanoantenna: silicon nanoparticle on a mirror. ACS Photonics 2018;5:1986–93.
[160] Nagasaki Y, Hotta I, Suzuki M, Takahara J. Metal-masked Mie-resonant full-color printing for achieving free-space resolution limit. ACS Photonics 2018;5:3849–55.

[161] Ho J, Fu YH, Dong Z, et al. Highly directive hybrid metal-dielectric Yagi-Uda nanoantennas. ACS Nano 2018;12:8616–24.
[162] Decker M, Pertsch T, Staude I. Strong coupling in hybrid metal-dielectric nanoresonators. Phil Trans A Math Phys Eng Sci 2017;375:20160312.
[163] Yang G, Niu Y, Wei H, Bai B, Sun H-B. Greatly amplified spontaneous emission of colloidal quantum dots mediated by a dielectric-plasmonic hybrid nanoantenna. Nanophotonics 2019;8:2313–9.
[164] Yang Y, Miller OD, Christensen T, Joannopoulos JD, Soljačić M. Low-loss plasmonic dielectric nanoresonators. Nano Letters 2017;17:3238–45.
[165] Novotny L, Hecht B. Principles of nano-optics. Cambridge, Cambridge University Press, 2012.
[166] Ramezani M, Casadei A, Grzela G, et al. Hybrid semiconductor nanowire-metallic Yagi-Uda antennas. Nano Lett 2015;15:4889–95.
[167] Casadei A, Pecora EF, Trevino J, et al. Photonic-plasmonic coupling of GaAs single nanowires to optical nanoantennas. Nano Lett 2014;14:2271–8.
[168] Shibanuma T, Grinblat G, Albella P, Maier SA. Efficient third harmonic generation from metal-dielectric hybrid nanoantennas. Nano Lett 2017;17:2647–51.
[169] Wang H, Ke Y, Xu N, et al. Resonance coupling in silicon nanosphere-J-aggregate heterostructures. Nano Lett 2016;16:6886–95.
[170] Liu S-D, Fan J-L, Wang W-J, Chen J-D, Chen Z-H. Resonance coupling between molecular excitons and nonradiating anapole modes in silicon nanodisk-J-aggregate heterostructures. ACS Photonics 2018;5:1628–39.
[171] Lepeshov S, Wang M, Krasnok A, et al. Tunable resonance coupling in single Si nanoparticle-monolayer WS_2 structures. ACS Appl Mater Interfaces 2018;10:16690–7.
[172] Wang H, Wen J, Wang W, et al. Resonance coupling in heterostructures composed of silicon nanosphere and monolayer WS_2: a magnetic-dipole-mediated energy transfer process. ACS Nano 2019;13:1739–50.
[173] Verre R, Baranov DG, Munkhbat B, Cuadra J, Käll M, Shegai T. Transition metal dichalcogenide nanodisks as high-index dielectric Mie nanoresonators. Nat Nanotechnol 2019;14:679–83.
[174] Yan J, Ma C, Huang Y, Yang G. Tunable control of interlayer excitons in WS_2/MoS_2 heterostructures via strong coupling with enhanced Mie resonances. Adv Sci 2019:1802092.
[175] Wiederrecht GP, Wurtz GA, Hranisavljevic J. Coherent coupling of molecular excitons to electronic polarizations of noble metal nanoparticles. Nano Lett 2004;4:2121–5.
[176] Fofang NT, Park T-H, Neumann O, Mirin NA, Nordlander P, Halas NJ. Plexcitonic Nanoparticles: plasmon-exciton coupling in nanoshell-J-aggregate complexes. Nano Lett 2008;8:3481–7.
[177] Schlather AE, Large N, Urban AS, Nordlander P, Halas NJ. Near-field mediated plexcitonic coupling and giant Rabi splitting in individual metallic dimers. Nano Lett 2013;13:3281–6.
[178] Dintinger J, Klein S, Bustos F, Barnes WL, Ebbesen TW. Strong coupling between surface plasmon-polaritons and organic molecules in subwavelength hole arrays. Phys Rev B 2005;71:035424.
[179] Wang QH, Kalantar-Zadeh K, Kis A, Coleman JN, Strano MS. Electronics and optoelectronics of two-dimensional transition metal dichalcogenides. Nat Nanotechnol 2012;7:699–712.
[180] Gutiérrez HR, Perea-López N, Elías AL, et al. Extraordinary room-temperature photoluminescence in triangular WS_2 monolayers. Nano Lett 2013;13:3447–54.
[181] Zhao W, Ghorannevis Z, Chu L, et al. Evolution of electronic structure in atomically thin sheets of WS_2 and WSe_2. ACS Nano 2013;7:791–7.
[182] Cihan AF, Curto AG, Raza S, Kik PG, Brongersma ML. Silicon Mie resonators for highly directional light emission from monolayer MoS2. Nat Photonics 2018;12:284–90.
[183] Shcherbakov MR, Neshev DN, Hopkins B, et al. Enhanced third-harmonic generation in silicon nanoparticles driven by magnetic response. Nano Lett 2014;14:6488–92.
[184] Makarov S, Kudryashov S, Mukhin I, et al. Tuning of magnetic optical response in a dielectric nanoparticle by ultrafast photoexcitation of dense electron-hole plasma. Nano Lett 2015;15:6187–92.
[185] Xiong XYZ, Al-Jarro A, Jiang LJ, Panoiu NC, Sha WEI. Mixing of Spin and orbital angular momenta via second-harmonic generation in plasmonic and dielectric chiral nanostructures. Phys Rev B 2017;95:165432.
[186] Gao D, Shi R, Miroshnichenko AE, Gao L. Enhanced spin hall effect of light in spheres with dual symmetry. Laser Photonics Rev 2018;12:1800130.
[187] Wang K, Titchener JG, Kruk SS, et al. Quantum metasurface for multiphoton interference and state reconstruction. Science 2018;361:1104–8.
[188] Stav T, Faerman A, Maguid E, et al. Quantum entanglement of the spin and orbital angular momentum of photons using metamaterials. Science 2018;361:1101–4.
[189] Slobozhanyuk AP, Poddubny AN, Sinev IS, et al. Enhanced photonic spin hall effect with subwavelength topological edge states: enhanced photonic spin hall effect with subwavelength topological edge states. Laser Photonics Rev 2016;10:656–64.
[190] Peng S, Schilder NJ, Ni X, et al. Probing the band structure of topological silicon photonic lattices in the visible spectrum. Phys Rev Lett 2019;122:117401.